



Towards a more efficient exploitation of on-shore and urban wind energy resources

Research and Innovation Action

Call: H2020-ITN-2019-1

Call topic: MSCA-ITN-2019 - Innovative Training Networks

Project start: 1 November 2019

Project duration: 48 months

D1.4: Mesoscale and microscale ABL simulations: final public report (Work Package 1 final public report)

Executive summary

The atmospheric boundary-layer simulation technologies considering experimental and numerical approaches for atmospheric flows over flat and complex terrains as well as urban areas is examined in this document.

Partner in charge: UPM

Project co-funded by the European Commission within Horizon 2020
Dissemination Level

PU	Public	PU
PP	Restricted to other programme participants (including the Commission Services)	–
RE	Restricted to a group specified by the Consortium (including the Commission Services)	–
CO	Confidential, only for members of the Consortium (including the Commission Services)	–



This project has received funding from the European Union's Horizon 2020 research and innovation programme under grant agreement No 860101

Deliverable Information

Document administrative information	
Project acronym:	ZEPHYR
Project number:	860101
Deliverable number:	1.4
Deliverable full title:	Mesoscale and microscale ABL simulations: final public report
Deliverable short title:	ABLSimTech-SoA
Document identifier:	ZEPHYR-14-ABLSimTech-SoA-Work Package 1 final public report-Final-v1.0
Lead partner short name:	UPM
Report version:	v1.0
Report submission date:	31/07/2023
Dissemination level:	PU
Nature:	R
Lead author(s):	Baris Kale (VKI), Kartik Venkatraman (VKI), Mohanad Elagamy (UPM), Shubham Shubham (NTU)
Co-author(s):	
Status:	Final

The ZEPHYR Consortium partner responsible for this deliverable has addressed all comments received. Changes to this document are detailed in the change log table below.

Change log

Date	Version number	Author/Editor	Summary of changes made
06/01/2023	v1.0	Mohanad Elagamy (UPM)	Preliminary index created
26/07/2023	v1.1	Mohanad Elagamy (UPM)	Final version submitted to the coordinator

Table of Contents

1. INTRODUCTION	9
1.1 THE PLANETARY BOUNDARY LAYER.....	10
2. ATMOSPHERIC FLOWS	12
2.1 ON-SHORE & FLAT TERRAIN.....	12
2.2 COMPLEX TERRAIN.....	13
2.3 URBAN ENVIRONMENT	16
2.3.1 Urban morphology and surface roughness	17
2.3.2 Wind flow characteristics in the urban canopy layer	17
2.3.3 Wind-flow characteristics along rivers, seaside, and open areas	18
2.3.4 Numerical Simulations of Urban ABL flows.....	18
3. EXPERIMENTAL APPROACH	18
3.1 ABL MODELING IN THE WIND TUNNEL	19
3.2 VALIDATION APPROACHES	19
4. COMPUTATIONAL METHODS FOR ATMOSPHERIC FLOWS	20
4.1 GENERAL OVERVIEW.....	20
4.2 MACROSCALE	21
4.3 MESOSCALE	21
4.4 MICROSCALE	22
4.5 MESOSCALE NWP SIMULATIONS AROUND FLAT TERRAIN	22
4.5.1 Introduction	22
4.5.2 The Høvsøre test site experiments	22
4.5.3 Atmospheric boundary layer (ABL) flow modeling.....	24
4.6 MICROSCALE CFD SIMULATIONS AROUND COMPLEX TERRAIN.....	27
4.6.1 Introduction	27
4.6.2 Methodology.....	28
4.6.3 Key Conclusions	30
4.6.4 Synthetic turbulence generation.....	33
5. NUMERICAL WEATHER PREDICTION (NWP) MODELING	37
5.1 RE-ANALYSES, OBSERVATIONS, AND DATA ASSIMILATION	37
5.2 WEATHER RESEARCH AND FORECASTING (WRF) MODEL.....	37
5.2.1 Pressure-based vertical coordinate and flux-form variables	38
5.2.2 Governing equations	39
5.2.3 Map projections	40
5.2.4 Numerical solutions	41
5.2.5 Physical parameterizations.....	43
5.3 WRF-LES.....	45
5.3.1 Terra-incognita.....	45
5.3.2 Scale-adaptive 3D PBL schemes	46
6. CONCLUSIONS	47
7. ACKNOWLEDGMENTS	47

List of Abbreviations

EC	European Commission
DoA	Description of Action
ABL	Atmospheric Boundary Layer
PBL	Planetary Boundary Layer
CBL	Convective Boundary Layer
SBL	Stable Boundary Layer
AMETSOC	American Meteorological Society
NWP	Numerical Weather Prediction
LES	Large Eddy Simulation
GCM	Global Circulation Model
CFD	Computational Fluid Dynamics
DTU	Technical University of Denmark
IWES	Fraunhofer Institute for Wind Energy Systems
WRF	Weather Research and Forecasting
NREL	National Renewable Energy Laboratory
DAPPLE	Dispersion of Air Pollution and its Penetration into the Local Environment
RANS	Reynolds-Averaged Navier-Stokes
URANS	Unsteady Reynolds-Averaged Navier-Stokes
COST	European Cooperation in Science and Technology
ASCE	American Society of Civil Engineers
DNS	Direct Numerical Simulation
LBC	Lateral Boundary Condition
UQ	Uncertainty Quantification
PDF	Probability Density Function
SFS	Sub-filter Scale
SGS	Sub-grid Scale
AD	Actuator Disk
AL	Actuator Line
BEM	Blade-Element Momentum
FFT	Fast Fourier Transform
POD	Proper Orthogonal Decomposition
AR	Autoregressive
MA	Moving Average
ARMA	Autoregressive Moving Average
CTRWS	Continuous Time Random Walks
STG	Synthetic Turbulence Generation
CFSR	Climate Forecast System Reanalysis
GFS	Global Forecast System
NARR	North American Regional Reanalysis
NMM	Non-hydrostatic Mesoscale Model
ARW	Advanced Research WRF
WRFDA	WRF Data Assimilation
NCAR	National Center for Atmospheric Research
NCEP	National Centers for Environmental Prediction
RK	Runge-Kutta
MYNN	Mellor-Yamada Nakanishi Niino
QNSE	Quasi-Normal Scale Elimination
MYJ	Mellor-Yamada-Janjic
YSU	Yonsei University
ACM	Asymmetric Convection Model
BouLac	Bougeault-Lacarrere
MRF	Medium-Range Forecast

VKI	von Karman Institute for Fluid Dynamics
TKE	Turbulence Kinetic Energy
NBA	Nonlinear Backscatter and Anisotropy
EDMF	Eddy-diffusivity Mass-flux

List of Figures

1	Earth's atmospheric layers. Retrieved September 13, 2020, from https://unilaggeography2012.blogspot.com/p/gry-101-introduction-to-physical.html	9
2	The PBL and evolution of its sub-layers in time.	10
3	Schematics of roughness classes provided by Troen and Petersen. Retrieved from: (Troen & Petersen, 1989).	13
4	European land types, sketched by Troen and Petersen. Retrieved from: (Troen & Petersen, 1989).	14
5	The different microscale processes in an idealized valley. Taken from: (H. Fernando, Mann, Laginha Palma, & Lundquist, 2018): Upstream blocking, katabatic flow, anabatic flow, valley flows, gap flows, recirculation zones.	15
6	A typical urban environment is shown along with the various urban flow features such as flow speed-up, channeling, and sheltering. Taken from: (Butler & Dagnew, 2013).	16
7	Comparison of the rural and urban ABL. The urban ABL comprises of the urban canopy sublayer and the wake sublayer created by the urban canopy. Taken from: (Emeis, 2018).	17
8	Recommended domain length for multi-directional and one-directional simulations. Retrieved from: (Franke & Baklanov, 2007).	19
9	Different roughness elements in an ABL wind tunnel. Retrieved from: (Bendjebbas, abdellah el hadj, & Abbas, 2016).	20
10	Temporal and spatial scales of some atmospheric events. The darkened area depicts the characteristic atmospheric motions. Retrieved from: (T. R. Oke, 1987).	22
11	Schematic of the Høvsøre site when looking from the top, showing the wind turbines and instrumentation installed in the test site.	23
12	Nested domain configuration from the mesoscale WRF simulation of the Høvsøre test site.	24
13	A screenshot from Google Earth satellite imagery of Høvsøre, Denmark, with wind turbines and experimental means indicated by yellow pins.	25
14	Time series of instantaneous horizontal wind speed, wind direction, and temperature at 80 m from numerical results corresponding to WRF-d04, and 10 min average experimental data from the Høvsøre mast.	25
15	Wind roses of average wind speeds at the met mast location for the periods of interest.	26
16	Elevation map and locations of interest at Perdigao. Positions of the measurement towers in the SW ridge group are indicated with the + symbols, likewise NE masts are marked with the x symbol, and the masts in the inside valley group are indicated with black dots. PT-TM06/ETRS89 coordinate system, height above sea level.	28
17	Computational domain, Δh_t is the difference in the elevation height of the terrain.	29
18	Simulation results and experimental data for wind velocity on the Southwest ridge for a) Tower 20 (tse04) b) Tower 34 (rsw03) c) Tower 37 (rsw06). The locations of the masts are given in Fig 16.	31
19	Simulation results and experimental data wind velocity inside the valley for a) Tower 25 (tse09) b) Tower 22 (tse06). The locations of the masts are given in Fig. 16.	31
20	Simulation results and experimental data for wind velocity on the Northeast ridge for a) Tower 29 (tse13) b) Tower 10 (tnw10). The locations of the masts are given in Fig. 16.	31
21	Wind paths of air parcels passing through a sphere of 55 m radius placed on top of the ground at given met mast locations. Flow lines colored in green represent trajectories for wind coming from 231° at the inlet, while red and blue lines illustrate wind at the inlet from 227.5° and 234.5° correspondingly.	32
22	Perturbation tendencies added to u , v , and θ in space. Light and dark shades indicate positive and negative perturbations. Taken from: (J. Mirocha, Kosovic, & Kirkil, 2014).	34
23	Instantaneous contours of U velocity component at approximately 97 m above the ground for weakly convective flat terrain. The three panels on the left-hand side indicate unperturbed flow domains, while the contribution of the perturbed tendencies is shown on the right-hand side. Large panels show the coarse nested LES domains, whereas small panels are inner fine-scale LES domains. The dashed area represents the nested domain. Taken from: (J. Mirocha et al., 2014).	35

24	Instantaneous contours of horizontal velocity components for a convective WRF-LES case. (a) Non-perturbed, (b) periodic stand-alone, (c) point perturbation, (d) cell perturbation, (e) spectral inertial sub-range, and (f) spectral production range. Taken from: (Munoz-Esparza, Kosovic, Mirocha, & van Beeck, 2014).	36
25	Advanced Research WRF system components. Taken from: (Skamarock et al., 2019).	38
26	η coordinates in WRF-ARW Retrieved from: (Skamarock et al., 2019).	38
27	Some nest configurations for multiple grids. (a) Telescoping nests. (b) Nests at the same level share the same parent grid. (c) Overlapping grids(1): cannot be used when feedback is activated. (d) Overlapping grids(2): not allowed. Taken from: (Skamarock et al., 2019).	40
28	Isotropic map projections in WRF. (a) stereographic, (b) Mercator, and (c) Lambert. Source: (Floater & Hormann, 2014).	41
29	Horizontal and vertical grids of the ARW. Source: (Skamarock et al., 2019).	43
30	Interactions among various physical parameterization schemes. Taken from: (Dudhia, 2014).	44
31	Sketch of the energy spectrum $\phi(\kappa)$ in the horizontal plane where κ is wavenumber. Source: (Wyngaard, 2004).	46

1 Introduction

The atmosphere prolongs about 100 km from the Earth's surface to the beginning of the outer space. Regarding all the layers of the atmosphere, the most significant processes that directly affect the action of the atmosphere take place within the *Troposphere*, which is the lowest portion of the atmosphere (Fig. 1). Physical events such as wind motion in the vertical direction, reduction in the temperature with gradually increasing height, and moisture are among the major parameters that characterize the behavior of the troposphere. Also, the weather perpetually changes and mixes up the composition of the involved gases within this layer.

The most significant part of the troposphere is its closest part to the Earth's ground, named the *Planetary Boundary Layer (PBL)*, or sometimes referred to as the *Atmospheric Boundary Layer (ABL)* (details of the PBL are given in sub-section 1.1). It is because many atmospheric events such as rising thermals, plumes or roll vortices, which carry most of the turbulent fluxes of momentum (Garratt, 1992), turbulent transport of moisture and pollutants (C. H. Moeng, 2016), electric fields, and electromagnetic radiation take place herein.

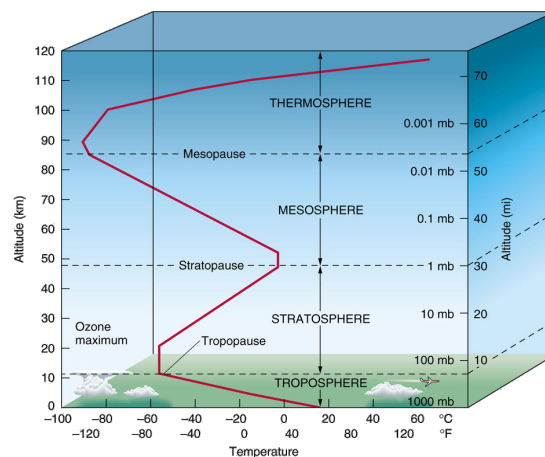


Figure 1: Earth's atmospheric layers. Retrieved September 13, 2020, from <https://unilaggeography2012.blogspot.com/p/gry-101-introduction-to-physical.html>

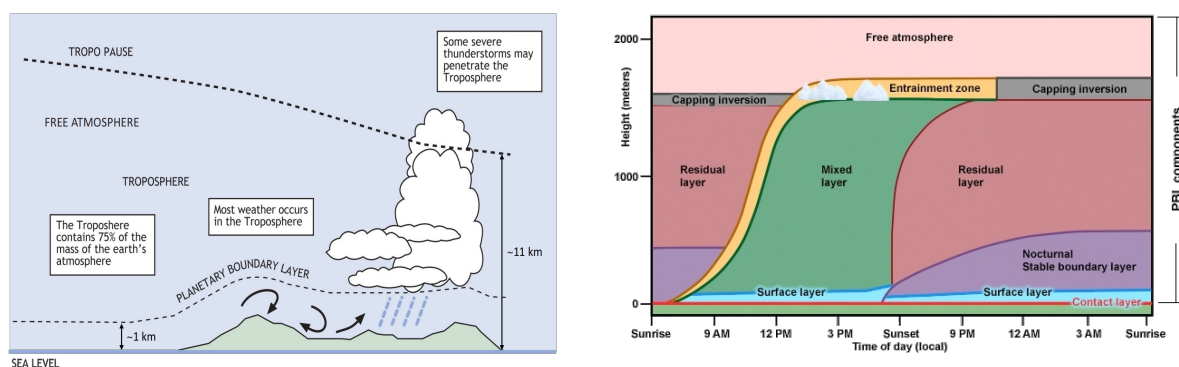
In order to examine the details of physical processes occurring inside the PBL, one has to consider not only observations or experiments (Garratt, 1992; Stull, 1988; Kaimal & Finnigan, 1994; Thomson, 1986; Faken, 2017) but also numerical modeling (Garratt, 1992; Stull, 1988; Chandrasekar, 2010; Andrews, 2010; Warner, 2011; Sommeria, 1983). Several methods have been used to investigate the structure of the ABL through the years. In particular, sensors installed on the meteorological towers (met masts) are used to collect weather data a few meters above the ground to the 200-300 m height above (Garratt, 1992). However, this effort is not enough to get the data from all over the PBL. For that reason, the use of an aircraft or a weather balloon is mandatory in some cases. Over the past years, remote sensing technologies, for instance, Doppler radars, acoustic sounders (sodars) and light radars (lidars), have been highly employed for atmospheric boundary layer observations (Stull, 1988). These types of technologies are more appropriate where in-situ measurements are pricey and more accurate where the atmosphere is affected by the radiation of the atmospheric quantity to be measured (Kaimal & Finnigan, 1994). Some other experimental studies of the ABL flows are done in laboratory tanks or ad-hoc wind tunnels (for details, see Chapter 3).

Another way of representing the structure and behavior of the PBL is numerical modeling. It has been generally preferred by researchers due to the economical issues of having reliable weather predictions (Chandrasekar, 2010). As stated by Moeng (C. H. Moeng, 2016), the statistical behavior of the PBL turbulence is mathematically modeled by a set of partial differential equations with suitable initial and boundary conditions. A huge amount of effort has gone into developing atmospheric models for the

investigation of the complex nature of weather using numerical methods (Chandrasekar, 2010). High-fidelity and state-of-the-art numerical methods are used to solve the fully-coupled set of mathematical equations. Plenty of *Numerical Weather Prediction (NWP)* models have been presented, starting from the well-known, classical one-dimensional eddy coefficient formulation to the advanced one or multi-dimensional models (Sommeria, 1983). In some models, grid sizes vary about a few meters in a *Large Eddy Simulation (LES)* in microscale through 1-25 km (mesoscale), ending up about 500 km in *Global Circulation Models (GCM)* in global scale (Garratt, 1992). Besides, coupling of *Computational Fluid Dynamics (CFD)* with larger-scale models is another commonly used numerical approach among researchers for addressing practical problems by using the inflow and boundary conditions of NWP models for CFD codes. However, it must be taken into account that the difference in the length scale of NWP and CFD models led both communities to model turbulence closure in a distinct way. Therefore, the conventional eddy closures used for CFD cannot be used directly, and their formulations must be altered regarding the physics of the atmospheric flows (Temel & van Beeck, 2017). Details of numerical modeling can be found in Chapter 4 and 5.

1.1 The planetary boundary layer

The planetary boundary layer is the lowest part of the troposphere with a depth that extends from tens to a few thousand meters above the Earth's surface (Fig.2a). The behavior of this layer is directly affected due to its contact with a planetary surface, and thus, the depth of the PBL is not always constant within a diurnal cycle. The thickness of the PBL is generally higher in day-time, whereas it tends to be lower in night-time. During the morning, the Earth's surface is heated up by the sun by radiation and conduction through the atmosphere. Convective motions enable to continuously grow a radiatively heated *unstable* PBL, so-called *Convective Boundary Layer (CBL)*, during the day and diminish the strongly statically *Stable Boundary Layer (SBL)* formed overnight because of radiational cooling and insolation. Horizontal and vertical scales within the PBL are of the order of the boundary layer depth, and PBL circulation timescales can reach up to a few hours (Garratt, 1992).



(a) The planetary boundary layer within the troposphere. Retrieved September 13, 2020, from <https://www.skybrary.aero/index.php/File:Troposphere.jpg> (b) Sub-layers of the PBL. Retrieved September 13, 2020, from <https://wasatchweatherweenies.blogspot.com/2017/10/lessons-in-boundary-layer-meteorology.html>

Figure 2: The PBL and evolution of its sub-layers in time.

Terrain complexity, radiation, surface friction, moisture, and wind velocity are one of the reasons for the change in the PBL depth through strong mechanical turbulence and convective activities. Turbulent motions are driven by wind shear and surface heating within the boundary layer and form a layer called *Mixed layer*, which is capped by a so-called *Entrainment zone* of intermittent turbulence (AMETSOC, 2012a). The mixed layer then slowly disappears, and the *Residual layer* begins to form because of the turbulence decay when the sun goes down. This cycle continues with the formation of a shallow stable boundary layer until sunrise. The *Free atmosphere* is located above the PBL, where wind flow can be assumed to be parallel to the isobars (i.e., geostrophic). On the other hand, the wind is strongly influenced by surface drag, and the assumption of geostrophic wind is not valid inside the PBL (AMETSOC,

2012b). There is a comparatively thin layer known as the *Surface layer* that is located just above the earth's surface. It is the lowest portion of the PBL, where flux remains almost constant. The depth of the surface layer is about 10 % of the whole PBL thickness (e.g., 100 m for a day-time PBL of about 1 km deep (C. H. Moeng, 2016)). All these sub-layers of the PBL are depicted in Fig. 2b.

The PBL dynamics and microphysics are controlled by the physical laws and equations of motion. Besides, these highly non-linear equations which govern the PBL are rather affected by the structure of the earth's surface and unremittingly changing characteristics of the free atmosphere. Moreover, the planetary boundary layer has a vital role in the transport of momentum, mass, and energy of the intrinsically turbulent mechanisms (Chandrasekar, 2010). These highly chaotic turbulent structures, which are extremely variable in strength, redistribute friction, moisture and heat within the boundary layer, as well as the other constituents such as pollutants.

The changes in vertical velocity, turbulence kinetic energy, near-surface temperature, and friction velocity in time do influence the planetary boundary layer parameters. When close to the ground, in other words, within the surface layer, the velocity scale is of a similar order of magnitude to the *friction velocity*.

$$u_* = \sqrt{\frac{\tau}{\rho}} \quad (1)$$

In Eq. 1, τ is the surface shear stress, and ρ is the air density. The logarithmic wind profile under neutral conditions is represented as the wind shear in the PBL and given as

$$u(z) = \frac{u_*}{\kappa} \ln\left(\frac{z}{z_0}\right), \quad (2)$$

where $u(z)$ is the wind speed at an altitude of z , κ is the von Kármán constant ($\kappa \approx 0.41$), and z_0 is the roughness length. In meteorology, the *potential temperature* is a commonly used variable and described as the temperature that an unsaturated parcel of dry air would have if brought adiabatically and reversibly from its initial state at temperature T and pressure p to a standard pressure level $p_0 = 1$ bar. It is formulated as:

$$\theta = T \left(\frac{p_0}{p}\right)^{\frac{R}{C_p}} = T \left(\frac{p_0}{p}\right)^{\frac{\gamma-1}{\gamma}}, \quad (3)$$

where R is the universal gas constant of air, C_p is the specific heat capacity at constant pressure, and γ is the ratio of the heat capacity of air. Another parameter is the *virtual potential temperature*, which considers the differences between the specific humidity in the air parcel and the surrounding air and formulated as:

$$\theta_v = \theta(1.0 + 0.61r - r_L). \quad (4)$$

r is the mixing ratio of water vapor, r_L is the mixing ratio of the liquid water in the moist air, and θ is the potential temperature. The virtual potential temperature can also be explained as the theoretical potential temperature of dry air, which would have the same density as moist air under the same conditions (Temel & van Beeck, 2017).

The *mixing ratio* of the water vapor is given knowing the vapor pressure e as follows:

$$r = \frac{0.622e}{p - e}. \quad (5)$$

To characterize the atmospheric stability, the *Richardson number*, Ri , is a widely used non-dimensional parameter and is defined as

$$Ri = \frac{\frac{g}{\theta_v} \frac{\partial \theta_v}{\partial z}}{(\frac{\partial U}{\partial z})^2 + (\frac{\partial V}{\partial z})^2}, \quad (6)$$

where g is the gravitational acceleration. The Richardson number can be physically interpreted as the ratio of energy production by buoyancy and shear. The threshold for the critical Richardson number is $Ri_c \cong 0.25$ for inviscid flow. If the actual Richardson number is less than its critical value, the flow

is assumed to be *dynamically unstable* and vice-versa. Another significant theory applied in the surface layer is the *Monin-Obukhov similarity theory* and explains the determination of the vertical profiles of the mean flow above the ground level. The Monin-Obukhov stability length, L , is formulated as:

$$L = -\frac{u_*^3}{\kappa \left(\frac{g}{\theta_w}\right) \left(\frac{q}{C_p \rho}\right)}, \quad (7)$$

and it is the altitude where the shear and buoyancy productions of turbulent kinetic energy are equal. In Eq. 7, θ_w is the wall temperature, and q is the vertical turbulent heat flux. The Monin-Obukhov length is more useful than the Richardson number because it can be assumed constant within the surface layer (Kaimal & Finnigan, 1994). It is used to determine the stability classes of the PBL. For example, if the surface heat flux is positive, which means that the temperature gradient normal to the surface is negative, the PBL is classified as *unstable*. Hence, the sign of the Monin-Obukhov length is negative for the convective boundary layer. An article published by Gryning et al. (Gryning, Batchvarova, Brümmer, Jorgensen, & Larsen, 2007) can be used for more details about atmospheric stability classes based on Monin-Obukhov length.

2 Atmospheric Flows

2.1 On-shore & flat terrain

On-shore flow is the movement of the cooler air towards the shore and is often followed by increased moisture. As a consequence of the energy exchange of cold-hot air, convective or stable internal boundary layers develop in a diurnal cycle. Since the sensible and latent heat fluxes are altered by the incoming flow, which happens naturally in on-shore flow, the thermal energy balance on the surface is not always constant, and a simple coupling has to be taken into account. This is more evident on the dry land, yet it is subtle over the land covered with vegetation (Kaimal & Finnigan, 1994). The most common examples of the on-shore flow are hurricanes and the daily sea breeze and are categorized under *local winds* (Orgill, 1981).

A terrain classification based on topographic features and roughness length was given by Troen and Petersen (Troen & Petersen, 1989) in the framework of the European Wind Atlas. According to the data obtained from a set of meteorological measurements from more than two hundred stations in the European Community Countries (Troen & Petersen, 1989), a terrain classification has been revealed, including four roughness classes characterized by a roughness length scale (Fig. 3) and five European landscape types (See Section 2.2).

The simplest type of flow over a flat surface is assumed to be homogeneous in the horizontal direction. This means that the statistical properties of the flow do vary with changing height and time yet are constant in the stream-wise direction. This assumption is called *horizontal homogeneity* and is crucial to understanding the Earth's complex structure and features. With the assumption of so-called local equilibrium, the advection of the flow quantities can be neglected. Partial derivatives along the horizontal axes can be canceled out by the assumption of horizontal homogeneity, and thus, governing equations can be simplified (Kaimal & Finnigan, 1994). A Terrain with short and uniform vegetation is a good example of flat terrain in real-world applications since advection terms have less impact on the mean flow and can be neglected.

The other assumption for the flat surface is the *stationarity*. As the name suggests, the time derivatives in the governing equations vanish because the change in time has no impact on the statistical properties of the flow. Although this condition is not applicable and is an idealized assumption as the behavior of the atmosphere changes in the long term, it allows the study of a particular application by treating it as a sequence of steady states (Kaimal & Finnigan, 1994). Using these two idealized conditions, one may apply empirical laws and theories of fluid dynamics to the atmospheric boundary layer problems. For instance, atmospheric flows over flat and homogeneous terrain in mesoscale can be modeled with a

basic 1D PBL model, and turbulent quantities of the flow can be evaluated using simple parameterizations.

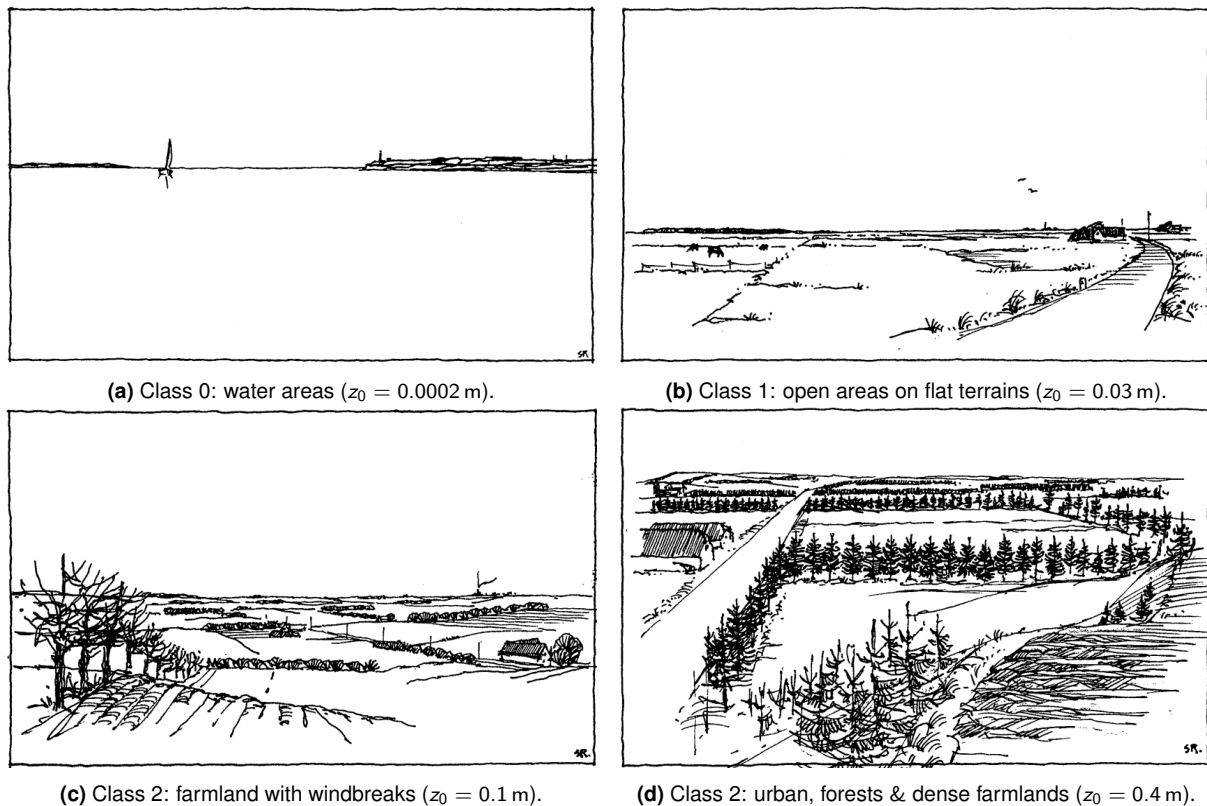


Figure 3: Schematics of roughness classes provided by Troen and Petersen. Retrieved from: (Troen & Petersen, 1989).

Another type of atmospheric flow over flat terrain is characterized by the flow circulation due to horizontal non-uniformity. The collapse of the uniformity leads to the formation of an internal boundary layer owing to the advective forces and allows for the creation of strong horizontal gradients, which are intrinsically resulting in 3D circulations. Land/sea breezes and urban heat island circulations are the most commonly encountered type of thermally-driven circulations due to the fact that the properties of the land and water surfaces are not similar (Finardi, Morselli, & P., 1989).

2.2 Complex terrain

Atmospheric flows over complex terrains have gained intensive popularity in the past decades and have been widely studied by many researchers (Kaimal & Finnigan, 1994; Troen & Petersen, 1989; Finardi et al., 1989). As stated by Troen and Petersen in European Wind Atlas (Troen & Petersen, 1989), the near-surface winds are only influenced by variable surface roughness, which leads to a non-homogeneous surface momentum flux and partially obstructs the wind in land *Type 1*, as shown in Fig. 4a. In addition to the impacts on the near-surface winds in land *Type 1*, hill-induced acceleration on the flow is a prominent property of *Type 2* lands. Though topography is not a dominant feature for previously introduced land types, it can be affiliated as the transitional effect from land *Type 2* to *Type 3*. Moreover, the PBL is strongly affected by the length scale of these orographic characteristics.

When air flows over a complex terrain, it starts digressing from its original path (e.g., flow acceleration, separation, and wake) and deforms slightly (e.g., streamline distortion). Due to the fact that some complex terrains where some rarely natural events (i.e., channeling) happen, some special flow systems

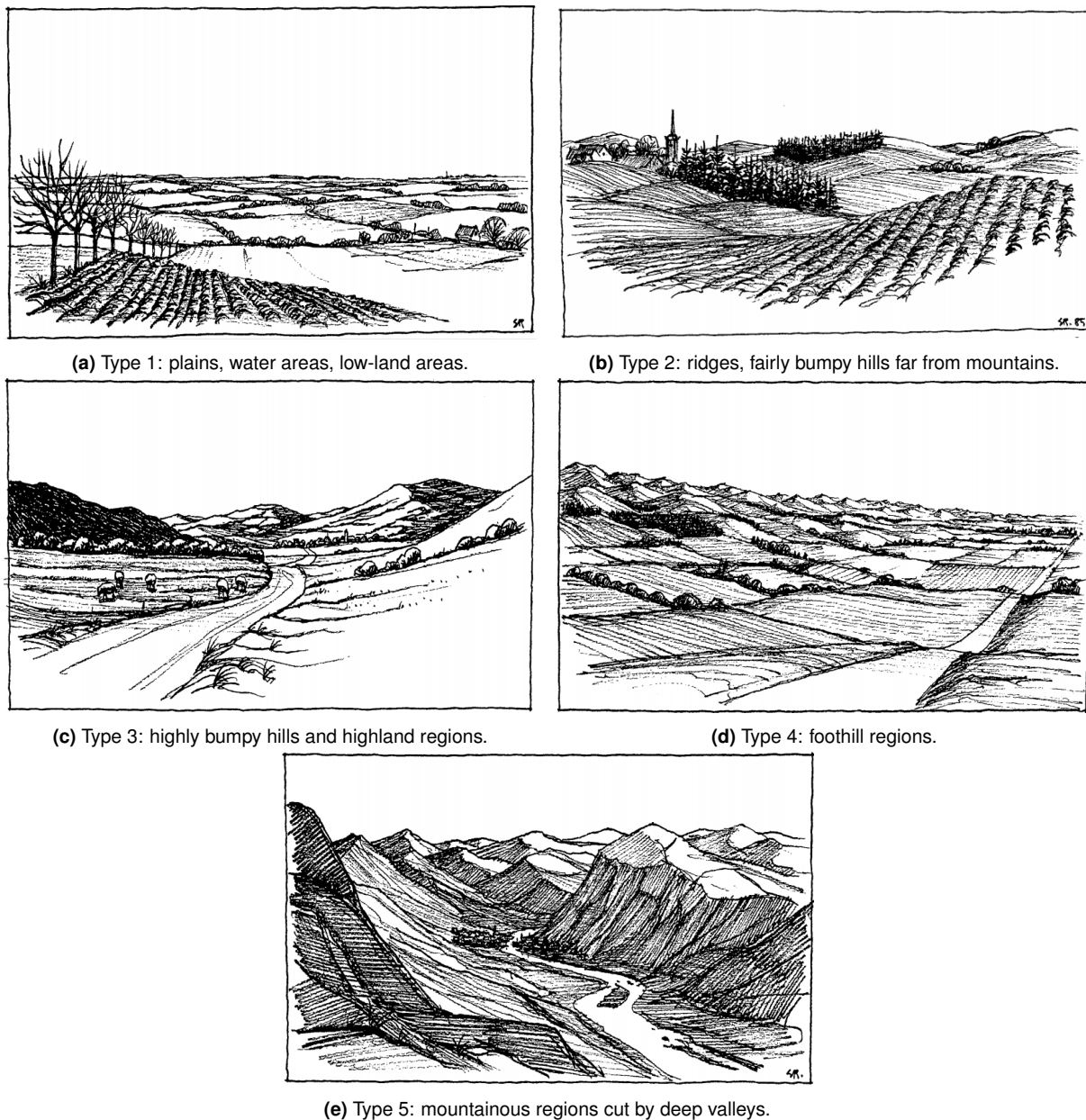


Figure 4: European land types, sketched by Troen and Petersen. Retrieved from: (Troen & Petersen, 1989).

such as *Föhn*, *Bise*, *Bora*, *Mistral*, and *Tramontana* may be seen (*Type 4*) (Troen & Petersen, 1989). The land *Type 5* can be an example of a complex region wherein valleys have a strong impact on the wind due to horizontal pressure gradients generated by differences in temperature distinction in air parcels, thus giving rise to *valley winds*, while *slope winds* are thermally-driven flows produced by the heat exchange between the air adjacent to the slope and the local ambient air (Whiteman, 1990).

Although the word *complex* evokes the morphological features of the terrain in the first sense, it is important to note that the vegetation covering the land surface (e.g., forest canopy) also plays a vital role in the complexity of the terrain, causing an increase of horizontal heterogeneity on several scales through the ABL (Kaimal & Finnigan, 1994). The surface boundary layer over terrain is highly affected by forests which strongly influence local winds such as low-level jets (Orgill, 1981). The physics and dynamics of the surface layer are generally vigorous because of the presence of strong sources/sinks of heat,

moisture, and momentum in a forest canopy. In a dense forest that would be fully covered by trees so neither sunshine nor wind is able to penetrate, the air at the mid-level remains cool and moist, whereas the warmer air sticks at the tree tops. Conversely, in a thin forest, the heat is able to penetrate into the forestry area. Therefore, convective motions such as updrafts and downdrafts occur more quickly. Similarly to the physics observed during day-time conditions, in a thin forest, highly strong temperature inversions develop overnight (Geiger, Aron, & Todhunter, 1995).

The lack of terrain availability in flat terrain pushes wind-farm developers to look for alternative sites along complex terrains. Winds in complex terrains are governed by the surface properties of the flow (land class/roughness) and the local elevation (hills, ridges, mountains) (Emeis, 2018). Local features such as ridges or canyons can also be advantageous for wind energy harvesting due to the creation of local flow accelerations. The wind field is channeled along valleys, with its direction being dependent on either the local pressure or temperature gradient. Mountains could act as partial obstructs, and certain features could result in flows along mountain gaps. The uneven heating of mountain slopes also causes slope winds (Steinacker, 1984). The heating and cooling is governed by the ratio of the active thermal surface area to the air mass. The pressure gradient caused by the differential heating along the valley is the driving factor for the winds. The different microscale flow features in an idealized valley are shown in Fig 5.

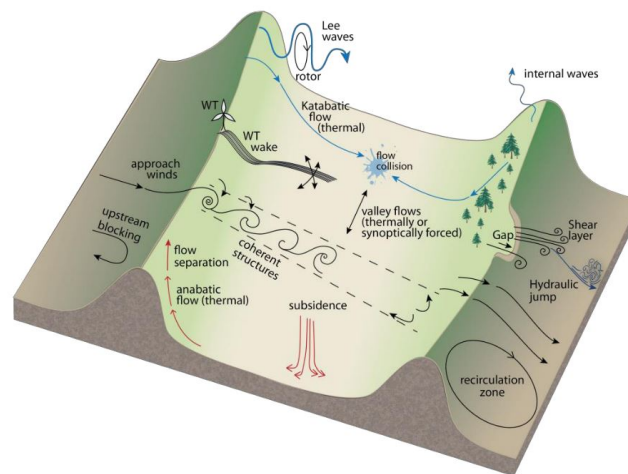


Figure 5: The different microscale processes in an idealized valley. Taken from: (H. Fernando et al., 2018): Upstream blocking, katabatic flow, anabatic flow, valley flows, gap flows, recirculation zones.

Complex terrains remain very challenging areas to consider for wind farm siting due to the following considerations:

- Wind resource assessment certainly requires to account for the multitude of different temporal and spatial scales;
- Wind farm modeling requires a more advanced approach than commonly used cost-effective linearized models, which cannot handle complex phenomena (i.e., flow separation);
- Wind-turbine noise propagation can be strongly affected by topography and the complex flow field. While wind turbines are often placed along ridges to benefit from the wind speed-up, noise issues may still remain a key environmental factor even in such areas that are usually found further away from urban communities.

2.3 Urban environment

The airflow in the urban environment has been under investigation, both computationally and experimentally, for many years. The urban environment consists of various obstacles, such as buildings, trees, and other intricate structures, which cannot be analyzed individually. Cities and urban areas have large roughness elements and widespread sealed zones (Emeis, 2018). These arrangements affect the flow patterns considerably. Thus, despite several advancements, this remains to be one of the most complicated yet vital fields of study for the installation of wind turbines in an urban setting.

A major part of the urban setting consists of buildings that impart frictional drag to the airflow. Local swift changes are observed in the wind velocity due to the turbulence that is generated by the frictional drag. Furthermore, powerful wind eddies are generated due to the pressure difference between and along the building height. Additionally, the aerodynamics of an urban setting can also be influenced by the profile and the spacing of the building. Closely spaced structures generate greater form drag, resulting in the wind moving quickly over the top whilst forming lee eddies between them (similar to speed-up over hilltops). Flow channeling takes place between taller buildings and in street canyons in which the winds move at higher speeds, typically close to the ground (Blocken, Carmeliet, & Stathopoulos, 2007). These various effects can be seen in Fig. 6. This could be potentially exploited as a location for urban wind turbines.

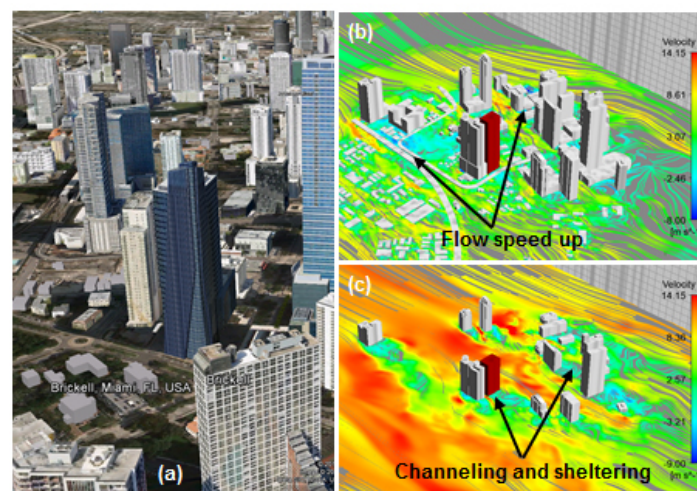


Figure 6: A typical urban environment is shown along with the various urban flow features such as flow speed-up, channeling, and sheltering. Taken from: (Butler & Dagnew, 2013).

The wind flow around an urban road canyon can be impacted significantly by the trees planted on the roadsides. The trees planted on and around the footpath serve as a good example of this, such that they decrease the wind speed considerably when they are perpendicular to the direction of the wind flow (M. Park, Hagishima, Tanimoto, & Narita, 2012).

Urban atmospheric boundary layers are substantially deeper than rural ABLs because of the stronger heat fluxes during the day (Theeuwes, Steeneveld, Ronda, Rotach, & Holtslag, 2015). The combination of increased possibilities for heat storage and reduced availability of moisture at the surface results in higher turbulence intensities. The increased heat storage during the day and reduced cooling during the night result in a phenomenon called 'urban heat islands'. This phenomenon can be attributed to reduced variability in ABL height during night and day. In recent years, there has been increasing attention towards urban environment aerodynamics. The studies are primarily centered around air pollution dispersion and wind flow close to pedestrians, such as the DAPPLE project: Dispersion of Air Pollution and its Penetration into the Local Environment (Arnold & ApSimon, 2004). To summarize, it is highly important to study the atmospheric flows in an urban environment to be able to harness wind energy to its maximum permissible potential and find the ideal locations.

2.3.1 Urban morphology and surface roughness

The surface roughness in an urban setting significantly influences the wind flow features, such as the turbulence intensity, surface drag, speed of the wind, and its profile (Ng, Yuan, & Chen, 2011). Detailed and accurate measurements of this characteristic are therefore required to predict the urban wind performance (T. Oke, 2004). At present, three principal methods are being used to make such measurements, including Davenport roughness classification (Wieringa, 2001), morphometric and micrometeorological methods (T. Oke, 2004). The surface type classification- Davenport is given according to various surface roughness estimates that are based on high-quality readings. Even though this method considers an extensive array of surfaces, it is not highly effective to define urban permeability in densely populated cities. The morphometric methods, in comparison with the micrometeorological technique, evaluate the aerodynamic properties by making use of empirical relations (Lettau, 1969). The development of morphometric methods with the help of GIS and remote sensing data enables a more cost-efficient evaluation of surface roughness over cities and urban areas.

This surface roughness layer runs from the surface to a height where the wind flow becomes homogeneous, which is about 2-5 times the height of a typical canopy element (M, Thom, & Edwards, 1980). Specific building arrangements affect the local airflow patterns and consequentially result in complicated features adjacent to the urban canopy elements present in this layer (Raupach, Thom, & Edwards, 1980). The different sub-layers of the urban ABL are shown in Fig. 7.

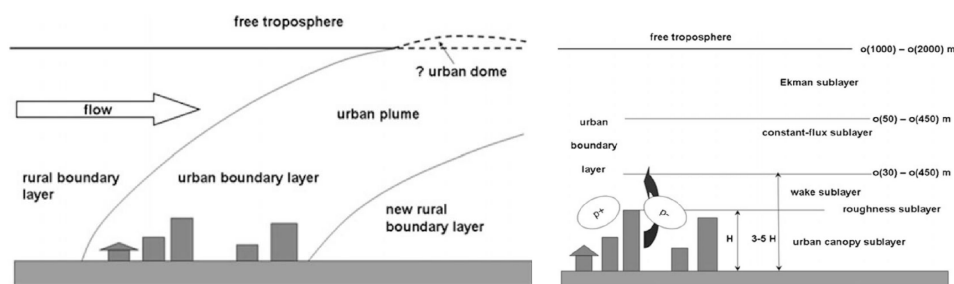


Figure 7: Comparison of the rural and urban ABL. The urban ABL comprises of the urban canopy sublayer and the wake sublayer created by the urban canopy. Taken from: (Emeis, 2018).

2.3.2 Wind flow characteristics in the urban canopy layer

The knowledge of airflow properties in an urban setup is incredibly important for various reasons:

- Analyzing the pollution dispersal in city paths (Kim & Baik, 2003);
- Evaluate the wind discomfort for foot-travelers (Janssen, Blocken, & van Hooff, 2012);
- Aids in studying the wind loading characteristics of small and medium-sized buildings;
- Wind resource assessment for urban wind turbines.

Researches show that airflow aerodynamics in an urban setting is very distinctive as compared to that of the turbulent boundary layer, which develops naturally above a homogenized rough surface (Salizzoni & Van Liefferinge, 2009). In this layer, the flow characteristics are influenced by the profile of the street or canyon and the structures, particularly in the zones where the building arrangement is compact, and a skimming flow pattern is generated (Razak, Hagishima, Ikegaya, & Tanimoto, 2012), whilst not being affected much by the properties of the oncoming flow.

2.3.3 Wind-flow characteristics along rivers, seaside, and open areas

To understand the urban environment in a better way, the effects of certain large-scale urban features, such as lakes, parks, and the seaside, are required to be studied (Spronken-Smith, Oke, & Lowry, 2000). The air circulation process governs the air quality in an urban setting (Wood & Pauscher, 2013), whilst the concentration of pollutants is also determined by the depth of the atmospheric boundary layer (Chou et al., 2007). Stream flows are found to carry pollutants, and wake flows are responsible for the accumulation of pollutants.

Studies have shown that water bodies serve as a vital source of ventilation in urban areas (Cho, 2010). These rivers act like urban street canyons, and the airflow characteristics change both in time and space close to the rivers. The turbulence around and over a water body depends on its roughness (Wood & Pauscher, 2013). Thus, the pollutant dispersal around the water body and the quality of air is considerably affected, considering the traffic on the roads along the water bodies. The wind speed is typically highest when it is directed in parallel along the river, while the aerodynamic drag results in a relatively low wind speed when the wind is approaching the water body perpendicularly. Thus, it can be concluded that the intricacy of the wind flow varies according to the changes in ground and building heights along its path.

2.3.4 Numerical Simulations of Urban ABL flows

Numerical simulations on the urban atmospheric boundary layer are primarily addressed to two important areas: wind conditions at the pedestrian level and dispersion of pollutants around buildings (Blocken, 2019). Different types of tools are used, such as RANS, LES, URANS, or hybrid RANS/LES, based on the required computational accuracy and available resources. LES models are better performing as they resolve the large vortical structures in the turbulent flow field. This is especially important for mass transfer in the dispersion study of pollutants. It also helps deduce "dynamic loading" on structures.

Several best practice guidelines are available for ABL simulations for choosing various simulation parameters such as boundary conditions, grid resolution, time step, and convergence criteria. Some of the main contributions were done as a part of the COST project Action 732 for 'Quality Assurance and Improvement of Microscale Meteorological Models' based on work of (Franke & Baklanov, 2007) and (Blocken, 2019). A few of the main best practices to be taken into account are as follows:

1. The blockage ratio (ratio of the area of the building to the area of the domain) of the flow is recommended to be a maximum of 3%;
2. The distances from the building to the sides, inlet, and top of the domain should be $> 5H$, with H being the height of the tallest building;
3. Distance from the building to the outlet is recommended to be greater than $15H$;
4. A high grid resolution in areas of large flow gradients, regions of interest for urban wind turbines;
5. First grid-lines near the wall should preferably be parallel/perpendicular to the wall by use of quadrilateral, hexahedral, or prism/wedge cells;
6. At least a second order or higher discretization scheme should be utilized.

3 Experimental approach

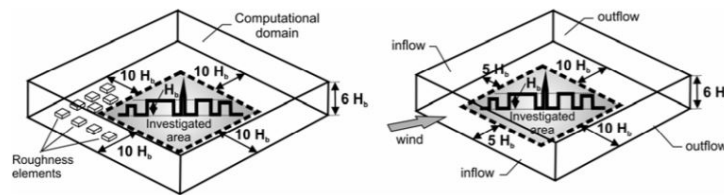


Figure 8: Recommended domain length for multi-directional and one-directional simulations. Retrieved from: (Franke & Baklanov, 2007).

3.1 ABL modeling in the wind tunnel

Specific wind tunnels are developed to simulate the lower part of the atmospheric boundary layer. The test section of such wind tunnels is usually long compared to aeronautical wind tunnels. The length of the test section is typically 10-15 times the section width to ensure that the flow is representative of a fully-developed ABL flow by the time it reaches the test region of interest. The airflow is non-uniform and has high turbulence intensity which is managed by adjusting the upstream ABL configuration, turbulence generator, and height of the roughness elements. Typical studies are performed in neutral conditions, although some heated wind tunnels exist to simulate the thermal effects due to surface heating. Wind tunnel data from experiments carried out under controlled inflow conditions is essential for validating atmospheric simulation models. Different kinds of roughness elements are utilized to produce the required wind speed profile and turbulence intensity spectrum. Elements include spires, barriers, carpets, and other distributed elements. Different combinations of these elements can be used to simulate different types of atmospheric boundary layers, as shown in Fig. 9.

The different requirements for ABL testing are as follows as highlighted by (Plate & Cermak, 1963)

- Geometric scaling of buildings and topographic features: A similar scaling factor should be conserved on the inflow profile (scaling $z_{0,real}/z_{0,WT}$). The integral length scale of the flow should also scale as the geometric scaling;
- Reynolds numbers threshold: It is difficult to match Reynolds numbers in practice. For buildings and terrains with sharp edges, the separation points are fixed, and a Reynolds number threshold is exceeded;
- Rossby number: It is defined as the ratio of inertial forces to Coriolis force due to the rotation of the earth. It is not very significant and is difficult to simulate in the wind tunnel;
- Matching the zero-pressure gradient found in the real world. Different roof adjustments are needed based on the type of terrain;
- Kinematic similarity: The velocity distribution should be simulated at least up to a height of 130 percent of the height of the highest building and ideally to the ceiling of the wind tunnel.

3.2 Validation approaches

The ABL wind tunnel should be capable of simulating flows representative of natural wind over different types of full-scale terrain. The minimum modeling requirements based on ASCE guidelines (ASCE, 1999) are as follows:

- The vertical distributions of mean wind speed and the intensity of the longitudinal turbulence component must be modeled;
- Important properties of atmospheric turbulence, such as the relevant length scales of the longitudinal turbulence component, must be produced;

- The longitudinal pressure gradient in the wind-tunnel test section should be sufficiently small.
- Surrounding buildings and structures and topographic features that influence the approach flow must be included in the model;
- For urban environments, all major buildings and structures within about 300 to 800 m from the site of study should be included in the scale model. The specific details of the model, such as the roof, can be reduced as the distance increases from the region of interest.

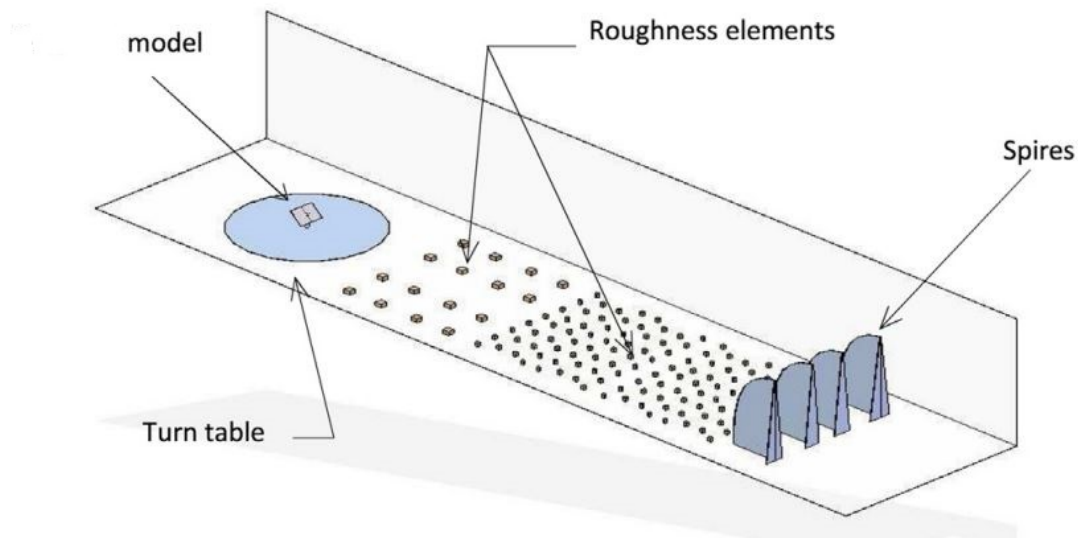


Figure 9: Different roughness elements in an ABL wind tunnel. Retrieved from: (Bendjebbas et al., 2016).

4 Computational methods for atmospheric flows

4.1 General overview

Despite the fact that field measurements are generally the best way of understanding the physics and the most common way of producing reliable data to validate an analytical approach or a numerical simulation of a certain problem, in the case of atmospheric flows, conducting an experimental study is not always practical and can be costly as well as difficult to reproduce the physical conditions of the problem (e.g., severe weather events). To overcome these research challenges related to ABL flow phenomena, computational methods based on numerical simulations of ABL flows either by solving the *Reynolds-Averaged Navier-Stokes (RANS)* equations or performing *Large Eddy Simulations (LES)* (Stull, 1988). The most accurate approach is to use *Direct Numerical Simulation (DNS)* models which capture all of the relevant turbulent eddies of motion, and thus no additional effort is needed to parameterize the effects of unresolved scales. Nevertheless, this is by far the most computationally expensive CFD modeling approach with computational restrictions for complex processes (Warner, 2011).

Individual applications of these RANS and LES equations are one of the ways of performing numerical simulations, and, in fact, a coupling algorithm can also be utilized by forcing or downscaling inflow and boundary conditions of larger-scale turbulent motions to microscale. However, the choice of correct simulation method depends on the length scales associated with the plenty of physical processes across the entire spectrum of the atmosphere, ranging from uni-dimensional eddies of planetary waves in global scale ($\sim 10^4$ km), fronts and cyclones in synoptic scale ($\sim 10^3$ km), thunderstorms, sea-land breezes, and mountain circulations in mesoscale ($\sim 1 - 10^3$ km), and the three-dimensional eddies occurring in

flows over complex terrains or urban canopies in microscale ($\sim 10^{-3} - 1$ km) (Temel & van Beeck, 2017). It should be stressed that atmospheric motions on large scales can substantially affect atmospheric boundary layer physics by creating strong turbulence. This is why reliable numerical modeling of the atmospheric flows for engineering applications requires additional attention to these turbulent physical phenomena (Temel & van Beeck, 2017). Time and space scales of various atmospheric events sketched by Oke (T. R. Oke, 1987) are shown in Fig. 10.

4.2 Macroscale

A *General Circulation Model (GCM)* which is used to represent *macroscale* features within the atmosphere, solves the same equations of motion as a *Numerical Weather Prediction (NWP)* model, which will be examined later in detail in Chapter 5; however, the temporal and spatial resolutions of the computational domain are adjusted to the problematic addressed by the simulation, and so are the modeling schemes involved. Global circulation models have been widely used for plenty of applications such as studying evolution as well as changes in the climate system and providing know-how for future climate states under numerous scenarios like carbon dioxide (CO_2) increase across the atmosphere with temporal resolutions of months or even years and coarser spatial resolutions ranging from 0.5° to 2.0° (Ringler, Heikes, & Randall, 2000). The part of a GCM model that depicts the general circulation is often called the *dynamical core*, and it has a strong effect on physical events in the atmosphere. These dynamical cores utilize similar mathematical equations to those described at the beginning of this section. Nevertheless, different numerical methods may be applied, such as finite-difference or spectral methods, in order to solve the governing equations used to delineate the evolution of mass, momentum, potential temperature, and an arbitrary number of passive scalars in time and space domains. Along with the Monin-Obukhov theory, the heat balance at the radiant surface is used to calculate the surface boundary conditions. As global circulation modeling has spatially low resolution in the vertical direction, a momentum flux is introduced at the surface instead of a no-slip boundary condition (Temel & van Beeck, 2017). The challenge of GCM is stability to be achieved in long-term and small perturbations in surface conditions or radiation input (McGuffie & Henderson-Sellers, 1997). There is also another atmospheric scale called *synoptic scale*. However, it is not examined in the scope of this report.

4.3 Mesoscale

The radar meteorologist Ligda (Ligda, 1951) was the first to introduce the term *mesoscale*, which has been commonly used among atmospheric scientists nowadays. Mesoscale can also be described as having a spatial scale in the horizontal direction smaller than the synoptic scale, yet larger than microscale and individual cumulus systems (Pielke, 2013). The vertical spatial scale stretches from tens of meters to the depth of the troposphere, and hydrostatic approximation to the vertical pressure distribution is applicable in mesoscale. The same set of governing equations as used in GCM is solved for limited spatial coverage, and the accuracy of mesoscale simulations is highly dependent on the temporal and spatial resolutions of the reanalysis data set obtained from GCM simulations which are applied as initial and boundary conditions. Weather events happening in mesoscale are generally disturbed by continuously occurring instabilities, forced thermal or topographic sources, and energy exchange due to either larger or lower scales of motions. The energy transfer from the microscale to the mesoscale is led to the formation of mesoscale convective systems. On the other hand, energy (heat) transfer from mesoscale to microscale is the reason for developing frontal circulations (Holton & Hakim, 2013). In order to achieve high-fidelity information on the turbulent properties of the flow, mesoscale/microscale coupling, for instance, nesting techniques, can be utilized so that the inflow and boundary conditions can be provided to the microscale models. Also, it is noteworthy to mention that temporal and spatial scales of the microscale models are refined with a nesting strategy (Munoz-Esparza, 2017).

4.4 Microscale

Microscale models represent three-dimensional features of the turbulent motion by solving 3D Navier-Stokes equations with appropriate boundary conditions applied at the wall, herein ground surface, unlike mesoscale and GCM codes. However, *lateral boundary conditions (LBC)s* can be derived either from incoming flow regarding the meteorological observations or a realistic large-scale forcing to the smaller ones provided by mesoscale simulations (Temel & van Beeck, 2017). Microscale modeling is often preferred due to its high accuracy, reliability, and fidelity in doing high-spatial-resolution simulations like LES. The complexity of systems aimed to be modeled using microscale models is caused by the ramifications of the models themselves.

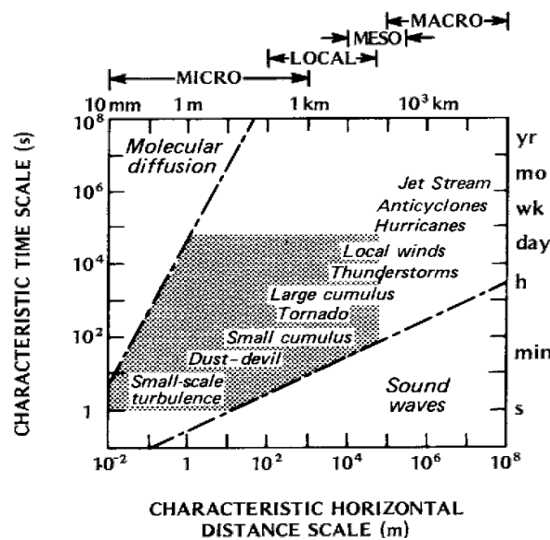


Figure 10: Temporal and spatial scales of some atmospheric events. The darkened area depicts the characteristic atmospheric motions. Retrieved from: (T. R. Oke, 1987).

4.5 Mesoscale NWP simulations around flat terrain

This section comprises parts of the Ph.D. thesis taken from (Kale, 2023) titled "ABL simulations with uncertain weather parameters and impact on WT performance and near-field noise".

4.5.1 Introduction

In order to investigate the atmospheric boundary layer conditions under realistic mesoscale forcing in flat terrain, the unstable ABL conditions observed at the Danish National Test Center for Large Wind Turbines at Høvsøre, Denmark, which is located in a relatively flat terrain by the western coast of Jylland, were chosen (Figure 11). The WRF model is utilized in order to simulate the period of interest with a multi-scale modeling approach. Three nested mesoscale domains, with the finest domain having a spatial resolution of 1 km, are used to dynamically downscale mesoscale flow features. The WRF model results have been compared with the available experimental data from the Høvsøre meteorological mast.

4.5.2 The Høvsøre test site experiments

The Høvsøre wind field experiment in 2006 was conducted, as part of a project supervised by Ejler Kristensen from Siemens Wind Power A/S, to measure the noise print of a Siemens 2.3 MW wind turbine



Figure 11: Schematic of the Høvsøre site when looking from the top, showing the wind turbines and instrumentation installed in the test site. The wind turbine considered in this work is encircled by the red circle. Experimental data was collected from a 116.5 m met mast shown in a white box. A screenshot from Google Earth satellite imagery of Høvsøre, Denmark. Met masts are shown by orange and yellow pins, whereas wind turbines are depicted by blue pins.

in flat and homogeneous terrain (Leloudas, 2006). The two-day field campaign took place in the coastal area of Høvsøre, Denmark, from May 30th to May 31st in 2006. The main goal of the experimental campaign was to perform noise measurements of a real-scale wind turbine operating in the atmospheric boundary layer using different pitch angles and rotational speed configurations.

Table 2: Instrumentation on the Høvsøre mast in Denmark (Peña et al., 2016).

Sensor type	Instrument	Height [m]
Wind speed	Risø P2546A cup anemometer	2, 10, 40, 60, 80, 100, and 116.5
Wind direction	Risø P2021A wind vane	10, 60, and 100
Relative humidity	F2920A Väisälä HMP45A RH/ T probe radiation shield	2 and 100
Temperature gradient	Risø P2642A sensor/ Risø P2029 radiation shield	2, 40, 60, 80, and 100 (relative to the lowest level)
Temperature (absolute)	Risø P2449A sensor/ Risø P2029 radiation shield	−0.05, 2, and 100
Pressure	P2717A Väisälä barometer PTB100	2 and 100
Turbulence	Metek USA1 F2901A sonic	10, 20, 40, 60, 80, and 100
Solar radiation	F2253C CM11 pyranometer	2

The weather data and relevant atmospheric parameters were also collected by experimental means, including sonic and cup anemometers, and wind vanes mounted on a 116.5 m tall met mast, also known as the Høvsøre mast, at varying heights (see Table 2). The weather data collected by the instruments were recorded and processed in real-time; the results were analyzed to provide valuable insight into the characteristics of the turbulent wind field, including its variability. The weather data collected from the Høvsøre mast, have also been used for many years to help improve the accuracy and reliability of numerical models used in wind resource assessment and wind power applications at Høvsøre, as well

as in the design and operation of wind turbines, and to increase the efficiency and reliability of wind power systems.

4.5.3 Atmospheric boundary layer (ABL) flow modeling

WRF model sensitivity to reanalysis dataset and PBL schemes Sensitivity analysis involves examining the response of the model output to changes in the input parameters. This type of analysis can help identify the most critical input parameters affecting the model's performance and provide insight into the underlying physical processes in order to perform reliable ABL flow simulations. When performing multi-scale simulations of atmospheric flows in wind energy studies, it is necessary to produce reliable and accurate ABL flow simulations for all domains from mesoscale to microscale.

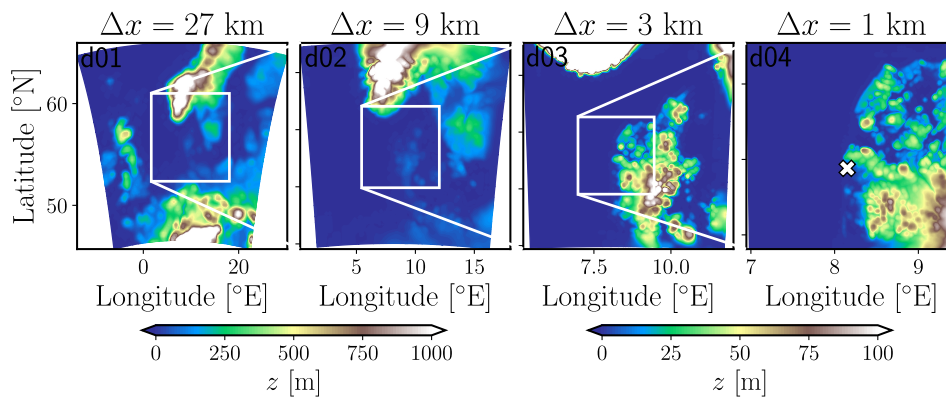


Figure 12: Nested domain configuration from the mesoscale WRF simulation. All nested domains centered on the Høvsøre test site are colored by terrain height where $z = 0$ m corresponds to sea level. The four domains have resolutions of 27 km, 9 km, 3 km, and 1 km. Domain dimensions and other model configuration parameters are given in Table 3.

A numerical error produced by any physical schemes used in multi-scale flow modeling can propagate across the nested domains, resulting in larger bias errors in atmospheric quantities in microscale flow analysis. This can cause further problems in the aeroacoustic modeling of the wind turbines, as the aerodynamic load will likely be incorrectly estimated.

With this regard, a sensitivity analysis based on four different PBL models, namely MYJ, MYNN, S-H, and QNSE, forced two different reanalysis datasets, that are ERA5 and GFS, was conducted to evaluate the accuracy of the WRF model in terms of factors such as horizontal wind speed, U , wind direction, β and temperature, T , at 80 m. The spatial and temporal resolutions of these datasets are as follows: $0.1^\circ \times 0.1^\circ$ and 1 h for the ERA5 and $1^\circ \times 1^\circ$ and 6-hour for the GFS reanalysis datasets, respectively.

Table 3: Domain dimensions and model configuration parameters for the sensitivity analysis of the ABL flow in the flat terrain of Høvsøre.

Domain	$N_x \times N_y \times N_z$	Δx [m]	Δz [m]	Δt [s]	Spin-up [hour]
d01	$81 \times 81 \times 58$	27000	~ 4	45	12
d02	$109 \times 109 \times 58$	9000	~ 4	15	12
d03	$133 \times 133 \times 58$	3000	~ 4	5	12
d04	$151 \times 151 \times 58$	1000	~ 4	5/3	12

Note. N_x , N_y , and N_z stand for the number of grid points whereas Δx , Δy , and Δz represent the spatial grid resolutions in the x , y , and z directions, respectively. Note that $\Delta x = \Delta y$ and Δz are set close to the values given in the table, because of WRF's terrain-following eta coordinate system in the vertical direction. Δt is the computational time-step size.



Figure 13: A screenshot from Google Earth satellite imagery of Høvsøre, Denmark, with wind turbines and experimental means indicated by yellow pins. The Høvsøre mast is encircled by a red ellipse. The white solid boxes indicate the boundaries of the finest WRF grid projected onto the test site ($\Delta x = \Delta y = 1$ km).

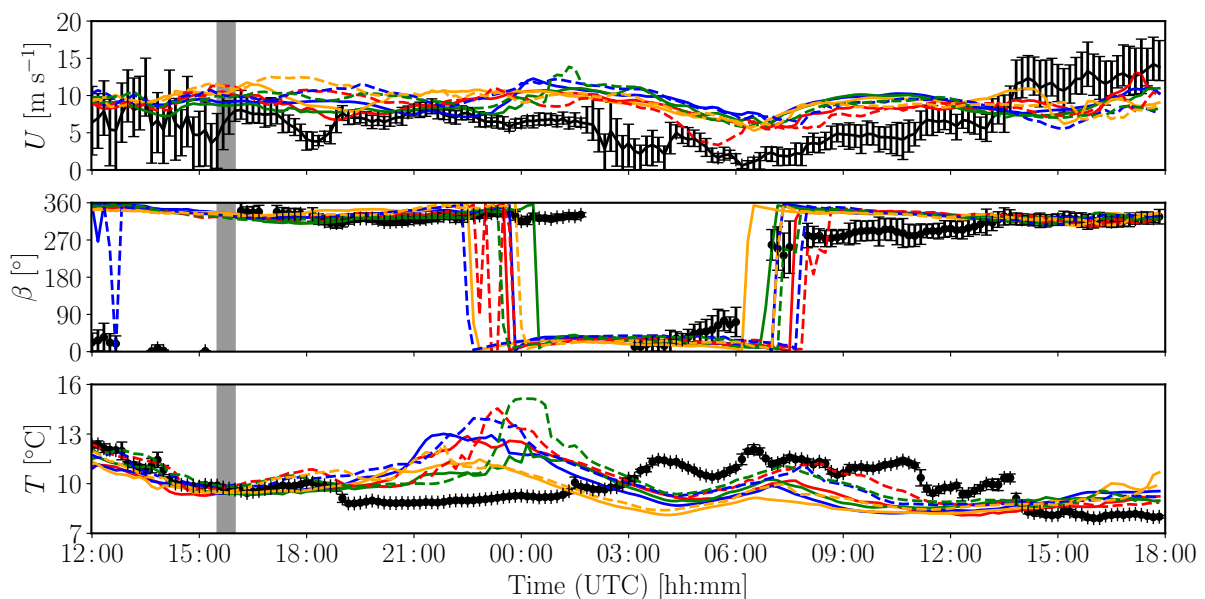


Figure 14: Time series of instantaneous horizontal wind speed, U (first row), wind direction, β (second row), and temperature, T (third row), at 80 m from numerical results corresponding to WRF-d04, and 10 min average experimental data from the Høvsøre mast. t (UTC) stands for Coordinated Universal Time in hours and minutes. The solid black lines with vertical bars correspond to experimental data with minimum and maximum values. The solid red, blue, green, and orange lines denote the predictions by the MYJ, MYNN, S-H, and QNSE models using GFS reanalysis data, respectively, whereas the dashed red, blue, green, and orange lines denote the predictions by the same models using ERA5 reanalysis data. The gray-shaded region depicts the period of interest in the mesoscale-microscale coupled wind turbine simulations (not given here).

Time series of above-mentioned atmospheric quantities were saved every 10 min and compared with 10 min-average weather data collected from the Høvsøre mast between 30/05/2006 12:00:00 (UTC) and

31/05/2006 18:00:00 (UTC), yielding a total analysis time of 30hours. The WRF results from the finest domain have been interpolated from the nearest grid points, using bi-linear and linear interpolation in horizontal and vertical space, respectively, to the Høvsøre mast location for comparison with the available experimental data.

A four-domain nested mesoscale simulation set-up shown in Figure 12 was used (details are provided in Table 3). An online mesoscale-microscale coupling approach with four one-way nested domains provided by the WRF model was employed. Physical parameterizations include the Kain-Fritsch scheme for cumulus (Kain, 2004), the Thompson scheme for microphysics (Thompson, Field, Rasmussen, & Hall, 2008), the Noah land surface model (F. Chen & Dudhia, 2001) and the Rapid Radiative Transfer Model for General Circulation Models (RRTMG) (Iacono et al., 2008). Revised MM5 surface layer scheme was used on all domains (Jiménez et al., 2012) for the S-H PBL model, whereas other PBL schemes were used with their own surface layer schemes. The model top was placed at 100 hPa (about 20 km in altitude) for the GFS reanalysis data and 20 hPa (about 33 km in altitude) for the ERA5 reanalysis data. For the upper 5 km of the domain, a Rayleigh damping layer was used to dampen the spurious waves that could be reflected from the model top. All domains were spun up for 12 h in order to achieve steady-state flow conditions and well-developed turbulent wind flow on all domains.

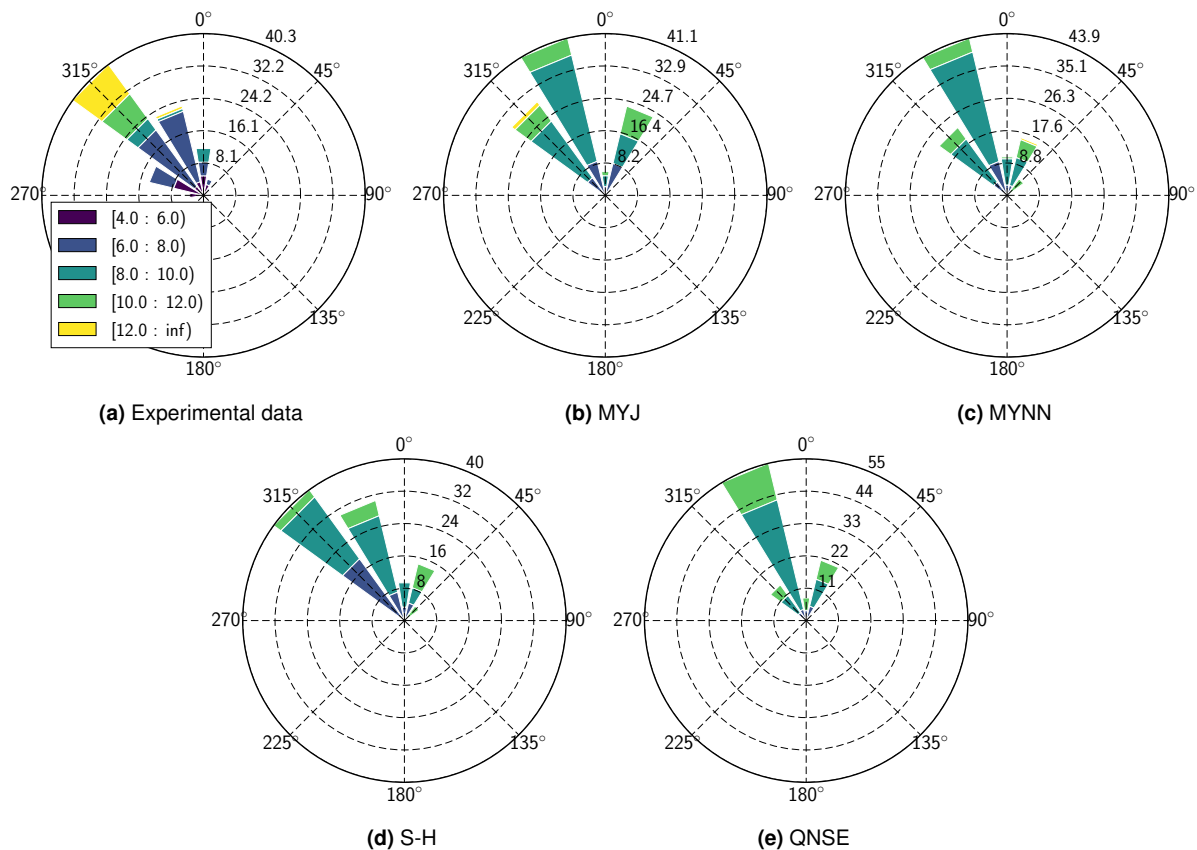


Figure 15: Wind rose of 10 min average wind speeds observed at the meteorological mast at 80 m for the periods between 30/05/2006 12:00:00 (UTC) and 31/05/2006 18:00:00 (UTC) (a) and wind roses of simulated 10 min instantaneous winds at 80 m at the same location and for the same time frame, using GFS reanalysis dataset, from the MYJ (b), MYNN (c), S-H (d), and QNSE (e) WRF PBL models. 0° and 270° denote the north and west directions, respectively. Increasing numbers in the radial direction represent the probability of the event occurring during the period of interest.

Results and key conclusions Due to the fact that the WRF PBL results are instantaneous values recorded every 10 min and experimental data consists of 10 min averages, no statistical metrics of the

WRF PBL sensitivity analysis with respect to the experimental data were calculated. Instead, 30 h time series of instantaneous U , β , and T from the finest domain of the WRF model and 10 min averages from the experimental data given in Figure 14 were compared qualitatively. The PBL model estimations of U , using ERA5 and GFS reanalysis, replicate a similar trend observed during measurements, with slight overestimation in the first 24 hours. As of 31/05/2006 at 14:00 (UTC), all PBL schemes underestimate the horizontal wind speed of about $\sim 4 \text{ m s}^{-1}$. For wind direction, all models forced with GFS and ERA5 reanalysis datasets agree reasonably well with the experimental data during the period of interest, with an overestimation of about $\sim 90^\circ$ between 07:00 (UTC) and 14:00 (UTC) on 31/05/2006. This might be due to the night/morning transition in which the characteristics and the state of the PBL alter, possibly creating changes in wind direction and wind speed. For temperature, all PBL schemes provide accurate enough estimates within the first six hours of simulation on 30/05/2006; however, large deviations were observed as of 18:00 (UTC) on the same day, yielding an average standard deviation of about $\sim 4^\circ\text{C}$ between 19:00 (UTC) on 30/05/2006 and 03:00 (UTC) on 31/05/2006. After, all models show a similar trend, underestimating the experimental data by $\sim 3^\circ\text{C}$ on average.

As stated by (Peña et al., 2016), according to a wind climate analysis conducted for the period between 2005 and 2013 at Høvsøre, northwest winds prevail in the Høvsøre region, so the North Sea affects most of the winds. North winds are rare; therefore, wakes from turbines at the Høvsøre mast location are rarely seen. Besides, the authors have revealed that unstable ABL conditions were mostly observed around midday while stable ABL conditions dominate the nighttime, as anticipated.

Figure 15 illustrates the wind roses of 10 min average wind speeds observed at the meteorological mast at 80 m over a period of thirty hours and WRF PBL model estimates of 10 min instantaneous wind speed at the same location and for the same time frame, using GFS reanalysis dataset. As illustrated in Figure 15a, $\sim 40\%$ of the prevailing winds at 80 m blew from the northwest (i.e., 315°) during this particular sampling period, justifying the previous wind climate observations reported in (Peña et al., 2016). The winds blew from the north $\sim 8\%$ of the time. Among all PBL model results shown in (Figures 15b to 15e), the S-H PBL model gave the best-prevailing wind direction and wind speed results, with least errors, compared to the experimental data and other PBL schemes either using GFS or ERA5 reanalysis dataset. Therefore, a combination of the S-H PBL scheme and GFS reanalysis dataset, with appropriate atmospheric physics parameterizations, has been used in further multi-scale simulations of wind turbine wake behavior at Høvsøre.

The sensitivity analysis based on mesoscale ABL flow modeling given in this section demonstrates the importance of determining the appropriate reanalysis dataset and PBL models, which significantly affect the accuracy of the model estimates of local weather conditions. Details of this study can be found in (Kale, 2023).

4.6 Microscale CFD simulations around complex terrain

This section comprises parts of the paper taken from (Venkatraman, Hågbo, Buckingham, & Giljarhus, 2023) titled "Effect of different source terms and inflow direction in atmospheric boundary modeling over the complex terrain site of Perdigão", Wind Energy Science Journal (2023).

4.6.1 Introduction

The objective of this work is to evaluate the impact of different physical source terms and turbulence models in Computational Fluid Dynamics (CFD) simulations of complex terrain. The study focuses on the comparison of simulation predictions with field measurement profiles at various groups of towers located at the Perdigão test site. The influence of canopy effects, Coriolis force, and two different sets of inflow profiles (one idealized set with a log-law velocity profile and one set of fully developed profiles based on a precursor simulation) are investigated. Furthermore, the influence of wind direction on the prediction of wind profiles is studied for the different case setups. An improved understanding of the importance of these phenomena will enable the development of more efficient and reliable tools to

perform wind simulations in complex terrain. An intensive observation period was carried out from 1 May 2017 to 15 June 2017 at the double ridge site of Perdigão, Portugal, by a consortium of American and European universities (H. J. S. Fernando et al.(2019)). The different meteorological masts used in this study, with heights of 60m and 100m, are shown in Fig.16. These masts can be grouped by their location on top of the Southwest ridge, inside the valley, or at the top of the Northeast ridge. A stationary period was found on the date of 4th May 2017 for the 30-minute averaged time interval of 22:00-22:30 using a tilt-corrected high-frequency dataset from NCAR-EOL. This period was based on the conditions at Tower 20 on top of the ridge, which corresponded to a Bulk Richardson number of approximately -0.03, qualifying as near-neutral conditions.

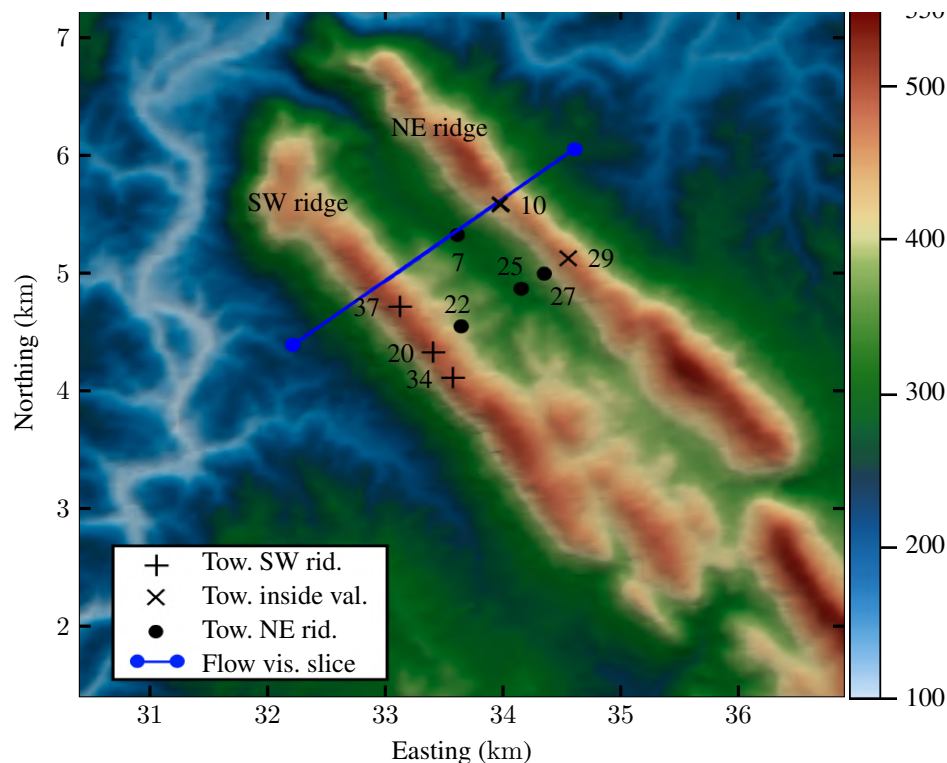


Figure 16: Elevation map and locations of interest at Perdigão. Positions of the measurement towers in the SW ridge group are indicated with the + symbols, likewise NE masts are marked with the x symbol, and the masts in the inside valley group are indicated with black dots. PT-TM06/ETRS89 coordinate system, height above sea level.

4.6.2 Methodology

The terrain is a 7.5 km × 7.5 km square centralized around a 100 m met-mast located on the Southwest ridge. Fig. 17 presents the computational domain and the dimensions are listed on the right side of the figure.

A cylindrical computation domain was developed, which provides the flexibility to simulate wind from any wind direction. The authors have successfully applied this approach in previous studies pertaining to urban areas (Hågbo, Giljarhus, and Hjertager (2021)) (Hågbo and Giljarhus (2022)). A smoothing region from complex to flat terrain was applied towards the outer boundaries, with a minimum radial distance of $15 \Delta h_t$. Several best practice guidelines have been formulated for grid generation for simulating complex terrain sites, such as by Sørensen et al. ((2012)) and Laginha Palma et al. ((2020)) and have been closely followed. The height of the domain is set to ten times the difference in the elevation height of the terrain, Δh_t , as recommended by Sørensen et al. ((2012)) when simulating wind flow over com-

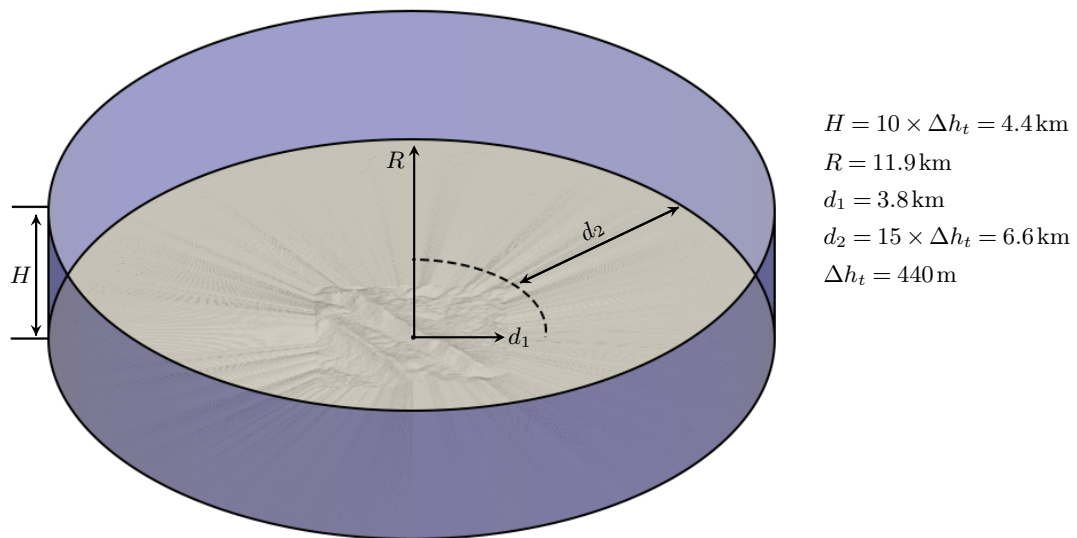


Figure 17: Computational domain, Δh_t is the difference in the elevation height of the terrain.

plex terrain sites. It consists of approximately 88 million cells and is produced with `terrainBlockMesher` developed by (Schmidt, Peralta, & Stoevesandt, 2012), capable of generating structured meshes over complex terrain exclusively consisting of hexahedra cells. The `terrainBlockMesher` tool uses a blending function to smooth the transition from the terrain patch to the outer cylindrical block. Around 50 radial block cells are defined, and a radial grading factor is used to enable stretching in the horizontal direction to cluster cells across the center of the domain and expand toward the boundaries. In terms of the number of cells per main direction ($N_x \times N_y \times N_z$), the mesh comprises $600 \times 600 \times 170$ across the terrain patch. The vertical mesh resolution is 24.5 m with uniform stretching applied across the entire domain. The minimal mesh height Δz next to the ground is close to 3 m. The average value of the wall y^+ is around 32 000. The mesh also follows the recommendation for having at least three cells from the ground to the height at the first sampling point for comparison with field measurements. The horizontal mesh resolution over the terrain was set close to 12.5 m. It satisfies the minimum resolution of 40 m recommended specifically for the Perdigão site by Laginha Palma et al. ((2020)). Terrestrial data was obtained from the Shuttle Radar Topography Mission (SRTM) database of the Perdigão field experiment (H. J. S. Fernando et al. (2019)).

All simulations have been conducted using the OpenFOAM (version 2012) toolbox. The simulations are steady-state and performed by solving the incompressible, three-dimensional steady Reynolds-averaged Navier-Stokes (RANS) equations with the finite volume method. Second-order discretization schemes were used for spatial discretization. The initial iterative convergence criteria were that the scaled residuals should drop four orders of magnitude for all flow variables as per the BPGs. Two steady-state solvers for turbulent flow of incompressible fluids have been used: `buoyantBoussinesqSimpleFoam` (BBSF) and `simpleFoam` (SF). All thermal effects are neglected in the simulations using both the solvers, such that the atmospheric stability of the simulated atmosphere is always neutral. In these simulations, the air density is assumed constant, and the gravitational force is neglected. The BBSF solver is capable of simulating the effect of buoyancy forces, but these source terms are set to zero for the present neutral case. However, in addition to solving the continuity equation and the momentum equation, which is solved using SF, the energy equation is also included, allowing for the modeling of non-neutral atmospheric conditions. Further details on the source terms and governing equations are given in (Venkatraman et al., 2023).

4.6.3 Key Conclusions

The results are discussed based on three groups of towers of interest: on top of the Southwest ridge, inside the valley, and on top of the Northeast ridge. The inlet profiles for all the simulations are calibrated to match the measured velocity magnitude and direction at 100 m at tower 20, which corresponds to an elevation of 573 m. Five different models are simulated comprising different source terms to account for the effects of the canopy, the Coriolis force and pressure gradient force, and two different inflow profiles. One idealized set with a log-law velocity profile, and one set of fully developed profiles based on a precursor simulation. Based on the flow topology, the predicted profiles are analyzed in terms of the different groups of towers on top of the ridges and inside the valley. The complex terrain site of Perdigão represents a large spatial variability of forest canopy and surface elevation, which contribute to variable flow topology at different met-masts. The key conclusions for different groups of towers are summarized as follows:

a) **For the towers on the Southwest ridge:** The region at the Southwest ridge is a zone of flow acceleration at the first oncoming ridge downstream of the inlet for wind coming from the Southwest. The inflow profiles are calibrated to closely match the wind speed and direction at Tower 20, as shown in Figure. 18. Using a canopy model (SF3) decreases the velocities near the surface and is a closer match with field data at Towers 34 and 37. Other models over-predict the velocity profile close to the ground. However, the canopy parameters need to be tuned as the surface heterogeneity is not considered, as the prediction accuracy varies at the different locations along the ridge.

b) **For the towers inside the valley:** The valley is a zone of flow re-circulation and comprises lower velocities and higher variability, which remains challenging for prediction models as shown in Figure. 19.

Moreover, large uncertainties are seen in the wind velocity, wind direction, and turbulent kinetic energy profiles for the field measurements. The prediction capabilities of the models vary with the location of the tower inside the valley. At all towers inside the valley, the SF1 model ($k-\epsilon$) provides the best prediction for wind velocity. Most models show large relative errors in wind speed and turbulent kinetic energy profiles, especially close to the ground.

c) **For the towers on the Northeast ridge:** The region at the Northeast ridge is a zone of flow acceleration downstream of the re-circulation zone from the valley. The canopy model (SF3) provides a strong under-prediction, while all other models provide a prediction within one standard deviation of the field measurements, as shown in Figure. 20. Predicting the extent of the re-circulation inside the valley and the re-attachment location plays a key role in the prediction profiles on the Northeast ridge. Significant turbulence is seen close to the ground in the field measurements and is under-predicted by most models.

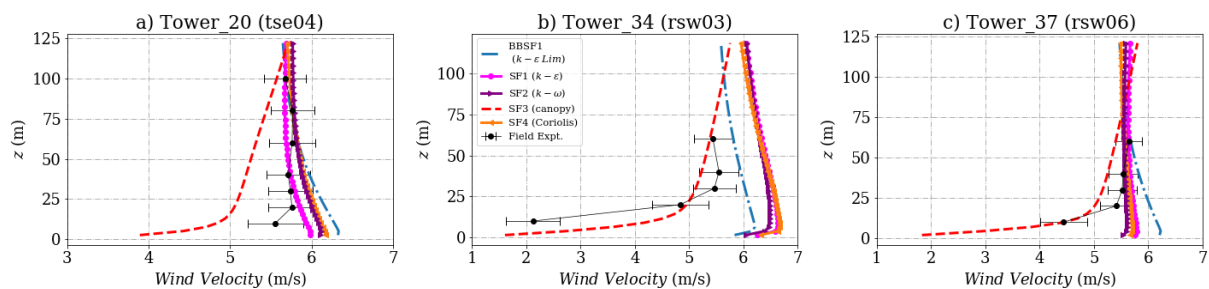


Figure 18: Simulation results and experimental data for wind velocity on the Southwest ridge for a) Tower 20 (tse04) b) Tower 34 (rsw03) c) Tower 37 (rsw06). The locations of the masts are given in Fig 16.

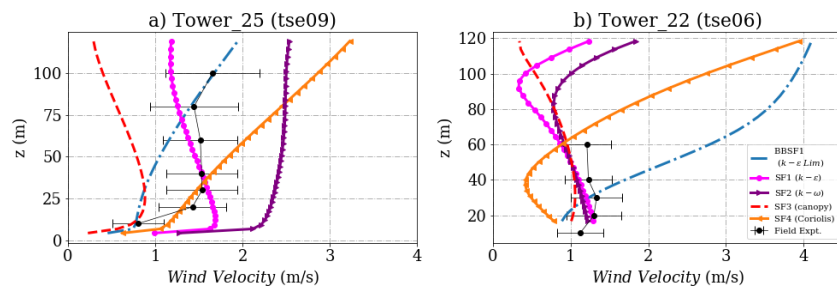


Figure 19: Simulation results and experimental data wind velocity inside the valley for a) Tower 25 (tse09) b) Tower 22 (tse06). The locations of the masts are given in Fig. 16.

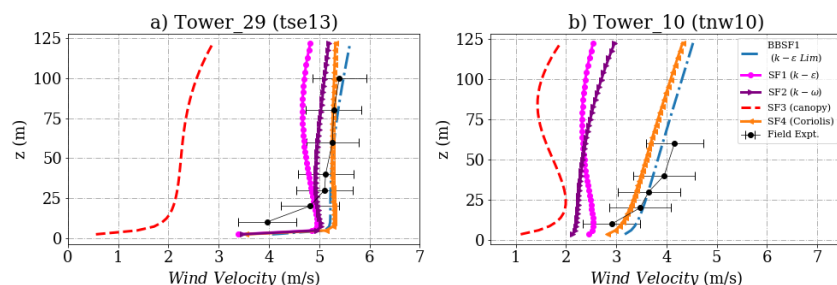
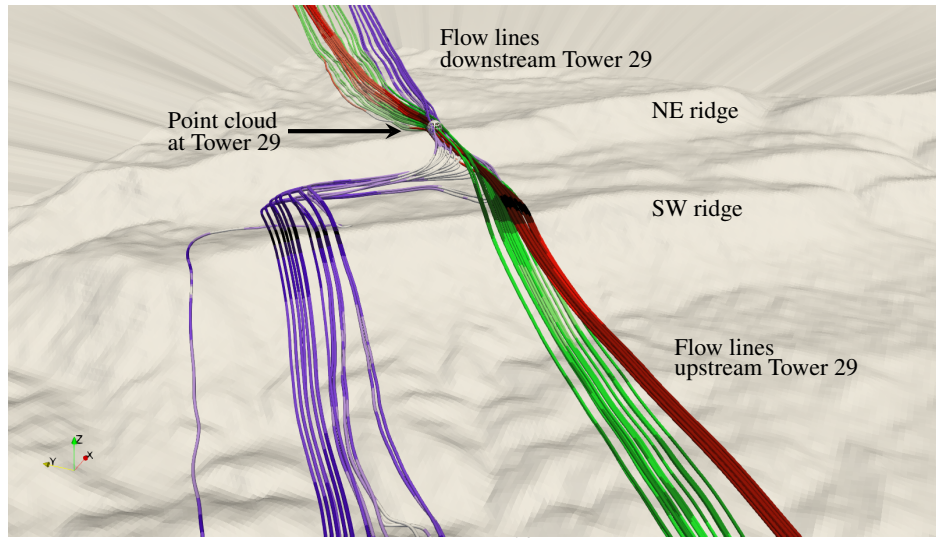


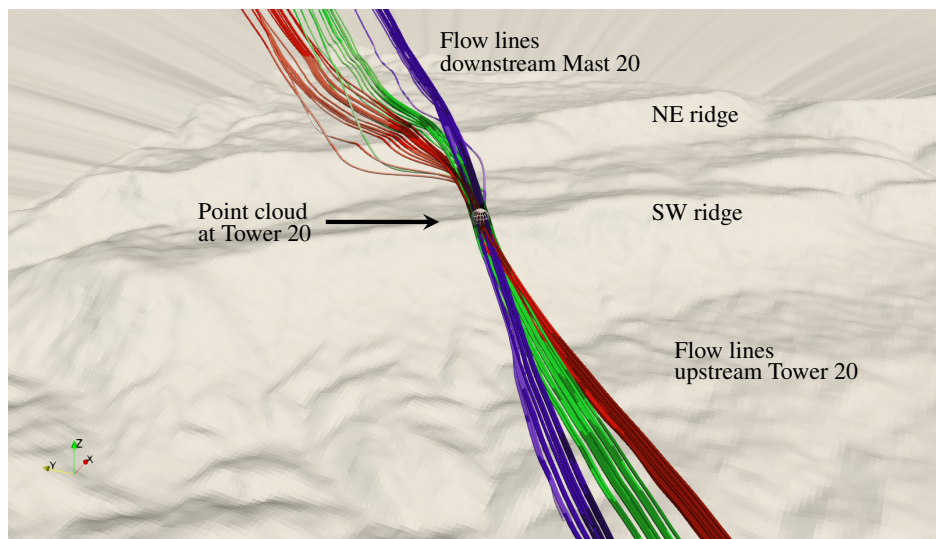
Figure 20: Simulation results and experimental data for wind velocity on the Northeast ridge for a) Tower 29 (tse13) b) Tower 10 (tnw10). The locations of the masts are given in Fig. 16.

d) **Influence of wind direction:** A significant difference in the wind profiles is seen using different inflow

directions as shown in Figure. 21. The extent of the re-circulation zone and the re-attachment downstream of the valley is different due to different trajectories taken by the inflow wind profiles coming from the South-West ridge. These uncertainties also depend on the turbulence model and source terms utilized.



(a) Tower 29.



(b) Tower 20.

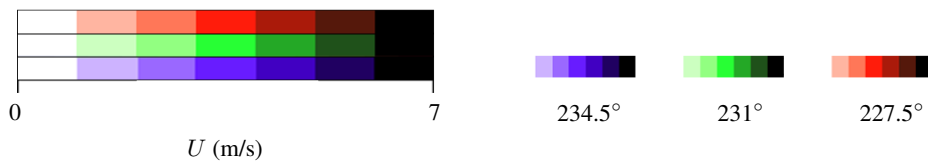


Figure 21: Wind paths of air parcels passing through a sphere of 55 m radius placed on top of the ground at given met mast locations. Flow lines colored in green represent trajectories for wind coming from 231° at the inlet, while red and blue lines illustrate wind at the inlet from 227.5° and 234.5° correspondingly.

4.6.4 Synthetic turbulence generation

Generation of wind velocity fields for aeroelastic simulations of wind turbines

The wind turbine design standards require simulation of the aeroelastic response of wind turbines for a specific large set of so-called "load cases". In these load cases, the wind turbine dynamics are simulated for specific wind field conditions, which are supposed to be a challenge to the operational integrity in general, and the structural integrity, in particular, of the wind turbine system. Additionally, the simulation of each load case must have a good level of statistical significance. To achieve this, a Monte Carlo simulation approach is followed. Therefore, the same load case is simulated several times for the same statistical definition of the corresponding velocity field but with a different random component. This strategy forces us to adopt a probabilistic description of the wind velocity field. This approach requires, first, that the wind field simulation guarantees the occurrence of the specific wind conditions defined in the standards (let us say a given level of turbulence intensity among others), and second, a fast enough simulation method since the number of load cases based aeroelastic simulations during the design and certification process of a wind turbine is very large.

Numeric Generation

As there are limitations to applying DNS, LES, and/or URANS for generating wind fields intended for the standard-based aeroelastic simulation of wind turbines, another method based on already existing statistical information is used for wind field simulation, which is the so-called numeric generation (Monahan, 2011). Numeric generation uses deterministic statistical characteristics of the actual wind field to generate synthetic stochastic wind fields. By using the numeric generation approach, only a few fluid dynamic constraints are imposed on the synthetic wind field, for instance, the continuity equation in incompressible conditions. Most frequently, simplifying statistical assumptions such as stationary are assumed. The spectral representation methods (SRM) and the sequential methods (SM) are considered as the major families in the numeric generation of wind fields to be used as input in the aeroelastic simulation of wind turbines. There are also other methods that are cited here for the purpose of completeness, such as continuous time random walks, modeling of energy cascade, and multi-scale reconstruction of time series. Although an agreed classification based on common names for the different numeric generation models lacks, an adaptation of the classification proposed in (Kleinhans, Friedrich, Schaffarczyk, & Peinke, 2009) is preliminary here adopted. Simplifying assumptions, such as statistical stationarity and/or statistical homogeneity and isotropy, are frequently used to reduce the mathematical complexity of the numeric generation models.

Spectral representation approach One of the most popular methods used for turbulent wind field simulation by means of numeric generation is the spectral representation method (SRM), which is theoretically supported by the Spectral Representation Theorem, (Grigoriu, 2002), which, in its basic form, states that a wide sense stationary one-variate and the one-dimensional random process can be represented an infinite sum of cosine terms with deterministic coefficients, which are obtained in terms of the power spectral density function of the random process, deterministic frequencies and random phases. Probably, the most widely used implementation of SRM was the adaptation of the Shinozuka model (Shinozuka & Jan, 1972) was proposed by Veers (Veers, 1988). The SRM presents two main computational challenges. The first one is to perform summations of the mentioned cosine terms (in general harmonic terms) in an efficient way. This is done using fast Fourier transform (FFT) techniques once the coefficients are obtained. The second one is to efficiently perform the decomposition of large cross-power spectral density matrices in the case of a multivariate process. This can be done through two main different approaches. The first method is using Cholesky decomposition, as in (Zhao & Huang, 2020). The second method uses proper orthogonal decomposition (POD) as in (Liu, Liu, & Peng, 2017). Different extensions of the SRM have been proposed for non-stationary wind fields (Xu et al., 2019).

Sequential approach The main idea of sequential methods is generating synthetic fields based on time series models, which involves discretizing the time domain into equal intervals. Under this framework, any value of the time series can be expressed as a combination of a deterministic component of past values plus a random term. The sequential approach is computationally efficient, and simulation can be restarted from a small amount of stored data. However, developing an optimal calibration technique for the model is the main challenge, together with the fact that the computational requirements may become high for large wind fields. There are three classical linear schemes for expressing the deterministic component: the autoregressive (AR) method, the moving average (MA) method, and the autoregressive moving average (ARMA) method. Mignolet and Spanos (Spanos & Mignolet, 1992)(Mignolet & Spanos, 1992) presented the early work on sequential simulation. Detailed analysis in the space domain of the auto-regression formula was proposed by Krenk (Krenk & Møller, 2019) to simulate stationary homogeneous isotropic wind field. According to the author, this approach shows increased efficiency. The weighted coefficients are calculated from the covariances matrices of the wind field at specific planes perpendicular to the mean velocity. Concerning MA models, the value of the optimum values for the coefficient matrices was presented by Spanos and Mignolet (Spanos & Mignolet, 1992). For ARMA models, the value of the optimum values for the weighted coefficient matrices was presented by Spanos and Mignolet (Spanos & Mignolet, 1992; Mignolet & Spanos, 1992). Deodatis (Deodatis & Shinozuka, 1988) presented how to deal with the non-stationarity using AR models to simulate one-dimensional and univariate Gaussian wind fields.

Synthetic turbulence generation (STG) methods in WRF framework The Weather Research and Forecasting (WRF) Model (Skamarock & Klemp, 2008) is a next-generation mesoscale model that was developed for both atmospheric research and numerical weather prediction. Using WRF, a multitudinous amount of work was done on studies of synthetic simulation of wind fields as well as realistic turbulent inflow generation in order to investigate the physical processes of turbulent flow in wind energy applications. When large-scale forcing is not enough, turbulence from quasi-turbulent mesoscale inflow is gently generated, and thus an external upwind fetch is needed in the flow domain. Even though there are various classical turbulent inflow generation methods in the literature, recently, some researchers have worked on the synthetic turbulence generation (STG) methods by introducing small perturbations on the tendencies of the flow properties, e.g., horizontal velocities u, v and the potential temperature, θ (J. Mirocha et al., 2014). This approach is relatively simpler than those classical turbulent inflow generation methods. They used the *Weather Research and Forecasting (WRF)* model, and these perturbations on the tendencies within the nested domains close to the domain boundaries are added to the prognostic equations of the WRF model. The perturbations are not employed very close to the parent domain boundaries since WRF uses a relaxation (sponge) zone between child nests and the mother domain. This relaxation zone is needed in order to accurately transfer inflow and lateral boundary conditions into the inner nests if a nesting technique is utilized. For instance, in the work by Mirocha et al. (J. Mirocha et al., 2014), they used 12 grid points before the location of the perturbed area (Fig. 22). These applied perturbations are sinusoidal and periodically updated in both horizontal and vertical directions.

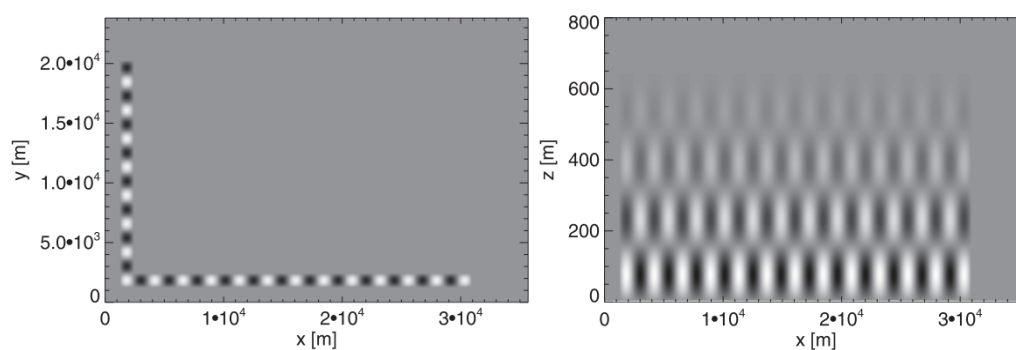


Figure 22: Perturbation tendencies added to u , v , and θ in space. Light and dark shades indicate positive and negative perturbations. Taken from: (J. Mirocha et al., 2014).

The perturbation field is stretched in the vertical direction until an upper level where capping inversion occurs. However, a uniformly spaced perturbation field is used in the horizontal direction since WRF uses homogeneous horizontal grid spacing. They simulated neutral flow over flat terrain, neutral flow over hilly terrain, and weakly convective flow over flat terrain by imposing perturbation on the tendencies and added them into the WRF's prognostic equations. An amplitude of $\pm 1000 \text{ kg s}^{-4}$ was found appropriate for each tendency yielding $(\Delta u, \Delta v; \Delta \theta) \cong \pm 2 - 3 \text{ (ms}^{-1}; \text{K)}$ and smaller values of the perturbations were not enough to generate accurate turbulent inflow while the larger ones created very large structures (J. Mirocha et al., 2014). Fig. 23 depicts an example of the unperturbed and perturbed flow domain for the weakly convective flow over flat terrain simulated by the Smagorinsky SFS model. It is found that using these perturbations within an atmospheric flow environment, e.g., horizontal velocities or potential temperature, the perturbed flow field can lead to an accurate turbulence state more quickly.

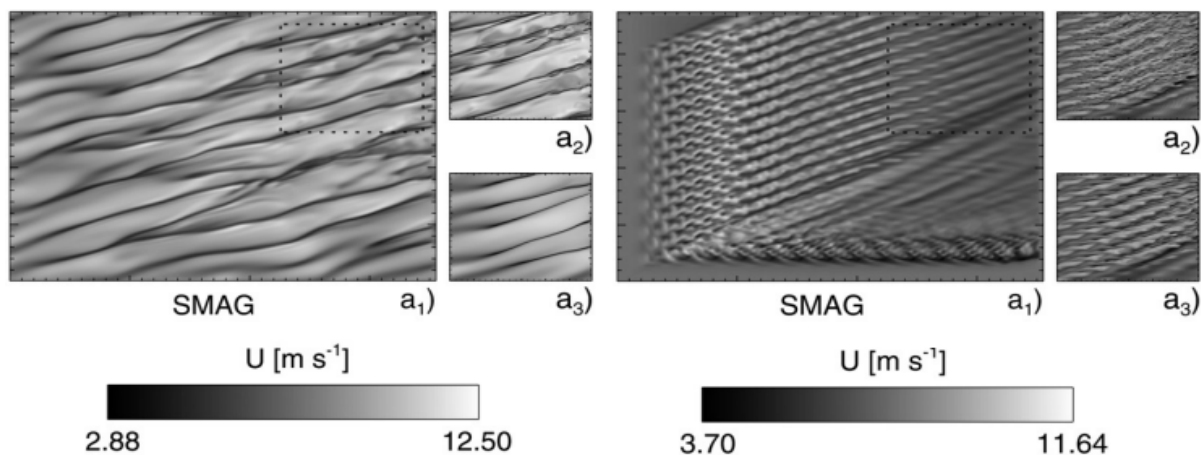


Figure 23: Instantaneous contours of U velocity component at approximately 97 m above the ground for weakly convective flat terrain. The three panels on the left-hand side indicate unperturbed flow domains, while the contribution of the perturbed tendencies is shown on the right-hand side. Large panels show the coarse nested LES domains, whereas small panels are inner fine-scale LES domains. The dashed area represents the nested domain. Taken from: (J. Mirocha et al., 2014).

Although synthetic turbulent inflow generation methods are generally based on the classical velocity perturbation, the use of temperature perturbations is another option among synthetic methods. For that reason, Munoz-Esparza et al. (Munoz-Esparza et al., 2014) have extended and further improved the work of Mirocha et al. (J. Mirocha et al., 2014) and proposed a new perturbation method regarding the perturbations on the potential temperature within a LES aspect. They proposed four different methods such as point perturbation method, cell perturbation method, spectral inertial sub-range method, and spectral production range perturbations. An application of these methods for a convective case simulated in the WRF-LES framework is shown in Fig. 3. The target of their work was to accelerate the turbulence transition from the larger scales to the smaller ones with a simpler mechanism rather than the classical ones, for example, imposing a fully-developed turbulent field of a pre-cursor simulation of the inflow of the current domain.

The first method, the point perturbation, is very simple compared to the other new methods and uses small pseudo-random perturbations uniformly distributed between $[-0.5, +0.5] \text{ K}$ at each grid point inside the perturbation zone (Munoz-Esparza et al., 2014). It was pointed out that a Gaussian distribution was also tested instead of uniform distribution. However, it resulted in very large local perturbations. The second method, the cell perturbation method, is also similar to the point perturbation. In fact, both methods use the same logic, yet the cell perturbation method slightly differs since the same perturbation amplitude is applied along a square, multi-dimensional cell (herein 8×8 grid points). The idea is based on rapidly dissipated energy at some high energy levels due to WRF's finite difference model discretization. The energy at these high wave numbers does not contribute to the generation of turbulence anymore, however, it plays a significant role in dissipation. The spectral inertial sub-range method is devoted to

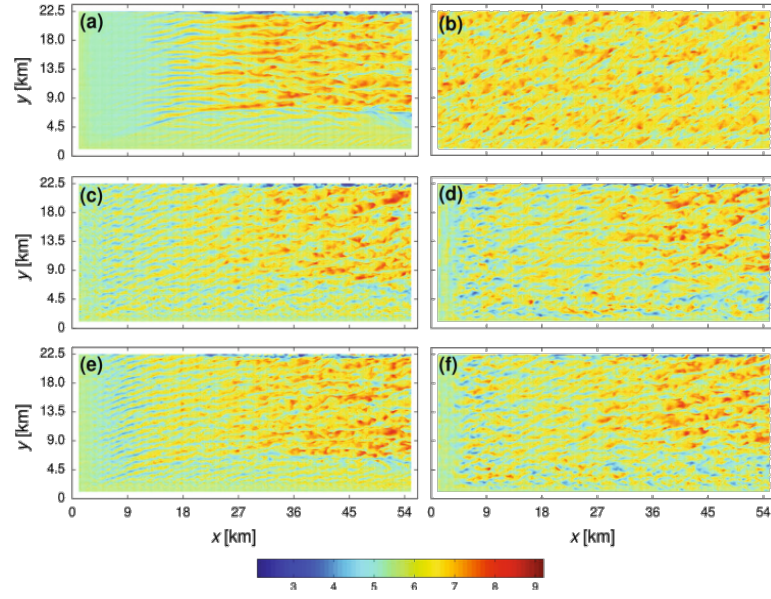


Figure 24: Instantaneous contours of horizontal velocity components for a convective WRF-LES case. (a) Non-perturbed, (b) periodic stand-alone, (c) point perturbation, (d) cell perturbation, (e) spectral inertial sub-range, and (f) spectral production range. Taken from: (Munoz-Esparza et al., 2014).

speed-up the generation of the inertial sub-range energy content. It uses three different modes, simply $k_1 < k_2 < k_3$, ranging from the inertial sub-range of 3D turbulence to the Kolmogorov $-5/3$ energy scale. The potential temperature perturbations are formulated as below:

$$\theta_{pert,i}(j) = a_i \left[\sin(k_1 j + p_{1,i}) + \left(\frac{k_2}{k_1} \right)^{-5/6} \sin(k_2 j + p_{2,i}) + \left(\frac{k_3}{k_1} \right)^{-5/6} \sin(k_3 j + p_{3,i}) \right], \quad (8)$$

where a_i is the random amplitude of the lowest mode perturbation, and it is uniformly distributed between $[-0.5, +0.5]$ K, $p_{1,j}, p_{2,j}, p_{3,j}$ are denoted random phases for every three modes, and uniformly distributed between $[0, 2\pi/L_i]$, where L_i is the horizontal length of the domain. i, j are the grid locations in both horizontal directions, respectively. Last but not least is the spectral production range perturbation method, in which the energy spectrum from a periodic simulation is used as a reference. Apart from the formula (Eq. 8), the spectral production range perturbation method based on the potential temperature perturbations is given below:

$$\theta_{pert,i}(j) = \sum_{k=k_{min}}^{k_{max}} a_k \sin(k_j + p_{k,i}); \quad (9)$$

where a_k is the amplitude and $p_{k,i}$ is the random phase for each node. $k_{max} = 2\pi/8\Delta x$, $k_{min} = 2\pi/L_i$ denotes the highest mode amplitude and uniformly changes between $-0.5, +0.5$ K. The rest of the amplitudes are found from the spectral distribution of the periodic simulation with random phases, which are distributed uniformly between $[0, 2\pi/L_i]$ (Munoz-Esparza et al., 2014).

To sum up, the cell perturbation method was found to be the best matching method in terms of achieving the fully-developed turbulence (Zhong, Cai, & Xie, 2019). It has been further improved by (Munoz-Esparza, Kosovic, van Beeck, & Mirocha, 2015) in order to account for large-scale forcing conditions for the neutral ABL. The aim of the perturbation methods provided by either Mirocha et al. (J. Mirocha et al., 2014) or Munoz-Esparza et al. (Munoz-Esparza et al., 2014) is to speed up the transition towards turbulence instead of superimposing a previously developed turbulent field as synthetic perturbation models do.

5 Numerical weather prediction (NWP) modeling

Numerical Weather Prediction (NWP) aims to forecast the state of the weather in the future. To do so, it uses current weather observations and processes these data with appropriate computational models based on the physical principles of the atmosphere. Numerous global and regional forecast models are used all around the world using existing observational data coming from remote sensing devices, weather satellites, and other observational equipment. Not only computational models but also these processed observational data, so-called *data assimilation*, are also significant in order to accurately predict the current state of the weather in terms of temperature, precipitation, and so on. This chapter summarizes the main features of the widely-used mesoscale code, the *Weather Research and Forecasting (WRF)* model.

5.1 Re-analyses, observations, and data assimilation

Re-analyses are by far the most used data set of weather and climate studies changing over time. The comprehensive information regularly provided by the re-analyses data set can extend over long time periods or even decades and cover the entire world from the Earth's ground to the upper parts of the atmosphere. In climate or weather forecasting research, re-analyses data are broadly used for monitoring and classifying the current climate conditions with those in the past and preparing climate predictions (e.g., Climate Forecast System Reanalysis (CFSR), Global Forecast System (GFS), North American Regional Reanalysis (NARR), etc). The acknowledged information from these data sets is produced via *data assimilation*, which combines observational data and the dynamical precept behind the system to provide a better estimation of the current status of the corresponding system than the raw data or computational model (Z. Zhang & Moore, 2015). Computational efforts used for climate modeling have not been aimed at including detailed data or the use of observational data in a computer simulation at the very beginning of the weather research, however, today's highly accurate and reliable computational models are capable of correct data assimilation have enabled to conduct simulations over longer timescales. On the other hand, some scientists are suspicious and have some doubts about the equality of the re-analyses data with the observations and measurements (Bosilovich et al., 2013). If the claim that Bosilovich and O'Neill (Bosilovich et al., 2013) declared in their article is correct, these differences can be related to the theory-based inference versus mirroring, reliance on forecasts, ill-posed inverse problems, and calibration and uncertainty, according to Parker (Parker, 2016). More information can be found in (Parker, 2016). However, in WRF, differences between the re-analysis data and observations are damped according to their perceived error (Wang et al., n.d.).

5.2 Weather research and forecasting (WRF) model

The Weather Research and Forecasting (WRF) Model (Skamarock & Klemp, 2008) is a next-generation mesoscale model that was developed for both atmospheric research and numerical weather prediction. It is a Fortran-based open-source code and its architecture allows parallel computation using two dynamical cores (solvers) (i.e., Non-hydrostatic Mesoscale Model (NMM), and Advanced Research WRF (ARW)), numerous physics options, pre- and post-processing, and a data assimilation (WRFDA) system (Skamarock et al., 2019). The ARW core was developed primarily at National Center for Atmospheric Research (NCAR) and the NMM solver was developed at National Centers for Environmental Prediction (NCEP). This section is devoted to a summary of key features of WRF-ARW dynamical core. The structure of the WRF-ARW core is shown in Fig. 25.

The WRF-ARW is an Eulerian solver and solves the fully compressible non-hydrostatic equation in flux form using a mass vertical coordinate. Several prognostic variables such as μ (column mass of dry air), u , v , w (velocity components), θ (potential temperature), and ϕ (geopotential). On the other hand, non-conserved variables such as T (temperature), P (pressure), and ρ (density) are found from the conserved prognostic variables. To summarize the general time and spatial discretization algorithm of

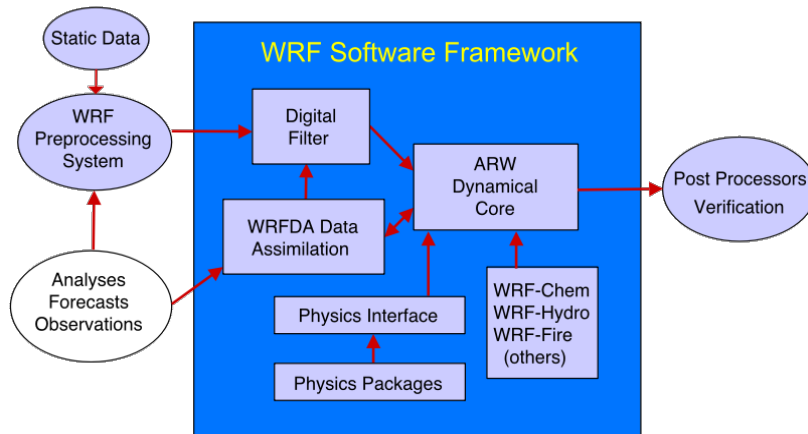


Figure 25: Advanced Research WRF system components. Taken from: (Skamarock et al., 2019).

the ARW solver, one can be said that it utilizes a split-explicit second-order time integration scheme for the acoustic and gravity-wave modes in addition to its main time discretization scheme based on second- or third-order Runge-Kutta time discretization algorithm for those which are meteorologically significant, i.e., low frequency, modes. The fully conservative flux divergence integration is handled with fifth-order upwind-biased advection operators as well as other options ranging from second-to-sixth order schemes (Skamarock & Klemp, 2008). Both ARW and NMM cores use the finite difference method to solve the transport equations on a staggered grid in the horizontal direction, which is different than those used in conventional CFD codes, and it is specifically called Arakawa-C grid (Adcroft, Hill, & Marshall, 1999). However, the vertical coordinates are based on dry hydrostatic pressure with vertical grid stretching (Skamarock et al., 2019).

5.2.1 Pressure-based vertical coordinate and flux-form variables

A terrain-following hydrostatic-pressure-based vertical coordinate system, η , i.e., a mass vertical coordinate system, is used for the formulation of the ARW equations and is defined as:

$$\eta = \frac{p_d - p_t}{p_s - p_t} \tag{10}$$

The η vertical coordinate system in Eq. 10 was first proposed by Laprise (Laprise, 1992), and the symbols p_d , p_s , and p_t refer to the hydrostatic component of the pressure of dry air, values of p_d at the surface and top of the domain, respectively. The values of η range from 0 to 1, where $\eta = 0$ corresponds to the upper boundary and $\eta = 1$ specifies the surface of the domain.

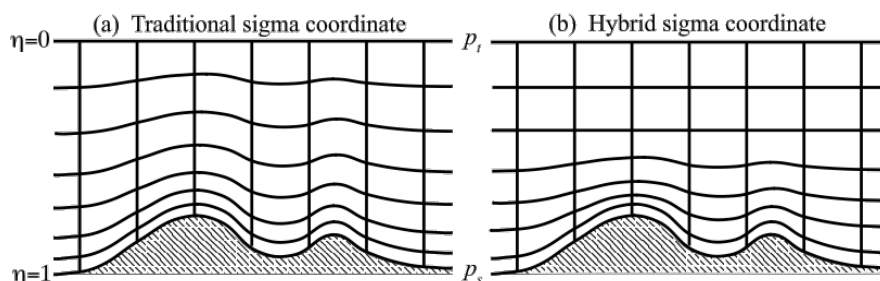


Figure 26: η coordinates in WRF-ARW Retrieved from: (Skamarock et al., 2019).

The first vertical coordinate depicted in Fig. 26, the traditional sigma coordinate, has been generalized in the newer versions of WRF code and took the *hybrid sigma coordinate* form represented on the right-

hand side of the Fig. 26b. The aim was to remove the influence of the terrain more rapidly than the traditional vertical coordinate system with the increasing height by employing a hybrid sigma-pressure vertical coordinate philosophy proposed by Park et al. (S.-H. Park, Skamarock, Klemp, Fowler, & Duda, 2013). Details of the hybrid sigma coordinate are given in (Skamarock et al., 2019).

In order to define the flux forms of the prognostic variables, it is convenient to introduce a vertical coordinate metric, μ_d , as:

$$\mu_d = \frac{\partial p_d}{\partial \eta}, \quad (11)$$

where $\mu_d \Delta \eta = \Delta p_d = -g \rho_d \Delta z$ is proportional to the mass per unit area within a grid cell. Following that, the flux forms of the prognostic variables can be defined as:

$$\mathbf{V} = \mu_d \mathbf{v} = (U, V, W), \quad \Omega = \mu_d \omega, \quad \Theta_m = \mu_d \theta_m, \quad Q_m = \mu_d q_m. \quad (12)$$

In Eq. 12, \mathbf{v} stands for the *covariant* velocities in three-dimensions, and $\omega = \dot{\eta}$ is the *contravariant* vertical velocity. The rest of the variables are the moist potential temperature, $\theta_m = \theta(1 + (R_v/R_d)q_v) \approx \theta(1 + 1.61q_v)$, and the mixing ratio of moisture variables, $Q_m = \mu_d q_m$, where q_m can be water vapor, cloud water, rainwater, etc. Lastly, despite the fact that $\mu_d \phi$ is not a conserved quantity, $\phi = gz$ can not be prescribed in flux-form though it is also a prognostic variable (Skamarock et al., 2019).

5.2.2 Governing equations

NWP codes solve fully compressible, non-hydrostatic Euler equations on staggered grids in terms of either mesoscale or microscale models. These flux-form transport equations including additional, non-conserved variables like $\phi = gz$ (geopotential), are given below.

$$\partial_t U + (\nabla \cdot \mathbf{V}u) + \mu_d \alpha \partial_x p + (\alpha/\alpha_d) \partial_\eta p \partial_x \phi = F_U \quad (13)$$

$$\partial_t V + (\nabla \cdot \mathbf{V}v) + \mu_d \alpha \partial_y p + (\alpha/\alpha_d) \partial_\eta p \partial_y \phi = F_V \quad (14)$$

$$\partial_t W + (\nabla \cdot \mathbf{V}w) - g[(\alpha/\alpha_d) \partial_\eta p - \mu_d] = F_W \quad (15)$$

$$\partial_t \Theta_m + (\nabla \cdot \mathbf{V}\theta_m) = F_{\Theta_m} \quad (16)$$

$$\partial_t \mu_d + (\nabla \cdot \mathbf{V}) = 0 \quad (17)$$

$$\partial_t \phi + \mu_d^{-1}[(\mathbf{V} \cdot \nabla \phi) - gW] = 0 \quad (18)$$

$$\partial_t Q_m + (\nabla \cdot \mathbf{V}q_m) = F_{Q_m}, \quad (19)$$

with the diagnostic equation for dry hydrostatic pressure, and the diagnostic relation for the pressure

$$\partial_\eta \phi = -\alpha_d \mu_d, \quad p = p_0 \left(\frac{R_d \theta_m}{p_0 \alpha_d} \right)^\gamma. \quad (20)$$

The variables that appear in the flux-form equations above are $\alpha_d = 1/\rho_d$, and α account for the inverse density of the dry air and inverse density of the air which refers to the full parcel density. It is fundamental to mention that the inner products of $(\nabla \cdot \mathbf{V}a)$ and $(\mathbf{V} \cdot \nabla a)$, where a is a generic variable, defined for ARW core are slightly different than in other CFD codes, and formulated as follows:

$$\nabla \cdot \mathbf{V}a = \partial_x(Ua) + \partial_y(Va) + \partial_\eta(\Omega a)$$

$$\mathbf{V} \cdot \nabla a = U \partial_x a + V \partial_y a + \Omega \partial_\eta a.$$

In Eq. 20, p_0 is the reference surface pressure, R_d is the gas constant for dry air, and $\gamma = c_p/c_v = 1.4$ is the ratio of the heat capacities of dry air whereas F_U , F_V , F_W , and F_{Θ_m} on the right-hand side of the equations 13-16 are the forcing terms due to model physics, turbulent mixing, spherical projections, and the earth's rotation (Skamarock et al., 2019).

Initial and boundary conditions Two types of simulation are available in the weather and research forecasting (WRF) code as *ideal* and *real* case scenarios. As it can be understood from the word "ideal", this type of case uses the idealized conditions, e.g., no mesoscale forcing on the inflow boundaries, while initial and lateral boundary conditions are provided from global three-dimensional re-analysis data for "real" case simulations. Top boundary conditions are prescribed as gravity-wave absorbing while the bottom boundary conditions are frictional or free-slip, which are controlled by the surface-layer parameterization schemes.

Nesting Horizontal nesting strategy in WRF allows the user to use a finer-resolution domain surrounded by a parent domain during a model run. Although a uniform grid can be enough to resolve synoptic scales providing effective forecasting data in larger-scale modeling, however, it may not be sufficient enough for some applications which require high spatial resolutions on smaller scales. For such circumstances, WRF is capable of employing a *nesting* technique to overcome the problem of information transfer from outer domains to the inner domains in which the spatial resolution of the grid is intrinsically enhanced. The inner domains are called *child grids* and get the initial and boundary conditions from their parent grids provided from suitable re-analysis data. The nesting technique in WRF offers two options: *one-way* and *two-way* nesting. In a one-way nest, the information is only interpolated from the coarse grid to the fine grid whereas the coarser grid information is updated by the fine grid, i.e., lateral boundary conditions are updated by the incoming info from the coarser domain and the feedback at each time step is recursively sent to the coarser domain. The coarse-resolution domains are separated from the finer-resolution grids with a relaxation zone near the boundaries to nudge the nest towards to coarser one. This zone also prevents the internal reflection of outward propagating waves at the boundaries (Basu, 2017).

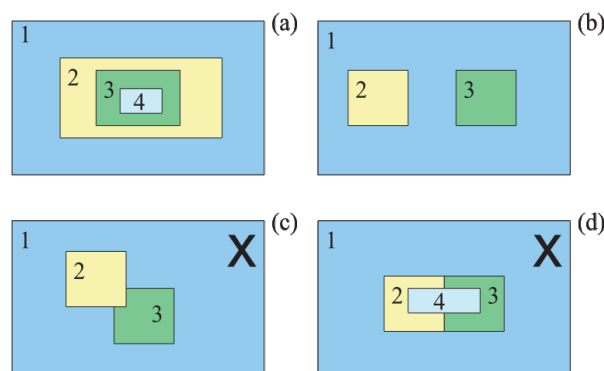


Figure 27: Some nest configurations for multiple grids. (a) Telescoping nests. (b) Nests at the same level share the same parent grid. (c) Overlapping grids(1): cannot be used when feedback is activated. (d) Overlapping grids(2): not allowed. Taken from: (Skamarock et al., 2019).

5.2.3 Map projections

Map projection methods in general are used to represent the globe's surface as a plane. However, herein NWP codes, these methods are used to solve the prognostic flux-form equations on planar surfaces. WRF supports four different projection types, such as the Lambert conformal, Mercator, polar stereographic, and recently latitude-longitude projections (Skamarock et al., 2019) and details are described in work of Haltiner and Williams (Haltiner & Williams, 1980). Although the Lambert conformal, Mercator, and polar stereographic projections are isotropic, meaning that $(\Delta_x/\Delta_y)|_{earth} = \text{constant}$ everywhere on the grid, the latitude-longitude projection is anisotropic (Details are not given here). The isotropic projections are shown in Fig. 27. Two scaling factors in the streamwise and spanwise directions are defined

in order to transform the governing equations:

$$(m_x, m_y) = \frac{(\Delta_x, \Delta_y)}{\text{distance on the earth}}; \quad (21)$$

where Δ_x and Δ_y are the horizontal grid spacings in x- and y-directions. It should be noted that these map scale factors have to be introduced to the governing equations by recasting the momentum variables as:

$$U = \mu_d u / m_y, \quad V = \mu_d v / m_x, \quad W = \mu_d w / m_y, \quad \Omega = \mu_d \omega / m_y, \quad (22)$$

and using variable definitions in Eq. 22, the governing prognostic equations in Eq. 13 - 19 can be rewritten as:

$$\begin{aligned} \partial_t U + m_x [\partial_x (Uu) + \partial_y (Vu)] \\ + \partial_\eta (\Omega u) + (m_x / m_y) [\mu_d \alpha \partial_x p + (\alpha / \alpha_d) \partial_\eta p \partial_x \phi] = F_U \end{aligned} \quad (23)$$

$$\begin{aligned} \partial_t V + m_y [\partial_x (Uv) + \partial_y (Vv)] \\ + (m_y / m_x) \partial_\eta (\Omega v) + (m_y / m_x) [\mu_d \alpha \partial_y p + (\alpha / \alpha_d) \partial_\eta p \partial_y \phi] = F_V \end{aligned} \quad (24)$$

$$\partial_t W + m_x [\partial_x (Uw) + \partial_y (Vw)] + \partial_\eta (\Omega w) - m_y^{-1} g [(\alpha / \alpha_d) \partial_\eta p - \mu_d] = F_W \quad (25)$$

$$\partial_t \Theta_m + m_x m_y [\partial_x (U \theta_m) + \partial_y (V \theta_m)] + m_y \partial_\eta (\Omega \theta_m) = F_{\Theta_m} \quad (26)$$

$$\partial_t \mu_d + m_x m_y [U_x + V_y] + m_y \partial_\eta (\Omega) = 0 \quad (27)$$

$$\partial_t \phi + \mu_d^{-1} [m_x m_y (U \partial_x \phi + V \partial_y \phi) + m_y \Omega \partial_\eta \phi - m_y g W] = 0 \quad (28)$$

$$\partial_t Q_m + m_x m_y \partial_x (U q_m) + \partial_y (V q_m) + m_y \partial_\eta (\Omega q_m) = F_{Q_m}. \quad (29)$$

These equations are solved together with the diagnostic equations (Eq. 20). Additionally, hence the name isotropic, the map-scale factors, m_x and m_y are the same in both streamwise and spanwise directions, i.e., $m_x = m_y = 0$.

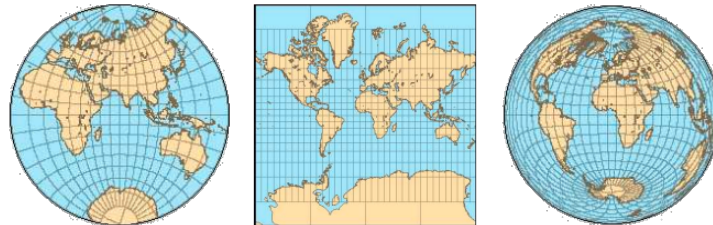


Figure 28: Isotropic map projections in WRF. (a) stereographic, (b) Mercator, and (c) Lambert. Source: (Floater & Hormann, 2014).

5.2.4 Numerical solutions

Temporal discretization A *time-split* integration scheme, meaning that *low-frequency* (meteorologically significant) modes are handled in a third-order Runge-Kutta (RK3) time discretization scheme, on the other hand, the *high-frequency* (acoustic) modes are considered within relatively smaller time steps, is used in the ARW solver to retain the solver's stability. In acoustic integration, not only gravity waves but also acoustic modes propagating in the horizontal direction are incorporated by a *forward-backward* time integration scheme. Furthermore, a vertically implicit scheme within acoustic integration is utilized for acoustic modes propagating in the vertical direction as well as oscillations due to buoyancy. The very basic idea behind this time-splitting algorithm is that the high-frequency acoustic modes would drastically restrict the computation time in the RK3 time step (Δt) (Skamarock et al., 2019). The time-split integration was first proposed by Klemp and Wilhelmson (Klemp & Wilhelmson, 1978), was enhanced by Wicker and Skamarock (Wicker & Skamarock, 2002), and was applied to the flux-form conservation equations by Klemp et al. (Klemp, Skamarock, & Dudhia, 2007). A predictor-corrector formulation is applied to the ordinary differential equations used in the RK3 scheme, formerly prescribed in the study

of Wicker and Skamarock (Wicker & Skamarock, 2002). Say prognostic variables used in the ARW solver defined as $\Phi = (U, V, W, \Theta_m, \phi', \mu'_d, Q_m)$, and the model equations as $\Phi_t = R(\Phi)$, then RK3 can be represented with the equations below which are the major steps of advancing the solution from the current time step to the next one:

$$\Phi^* = \Phi^t + \frac{\Delta t}{3} R(\Phi^t) \quad (30)$$

$$\Phi^{**} = \Phi^t + \frac{\Delta t}{2} R(\Phi^*) \quad (31)$$

$$\Phi^{t+\Delta t} = \Phi^t + \Delta t R(\Phi^{**}), \quad (32)$$

where Δt is the time step for the low-frequency modes, and superscripts refer to the next time levels. Perturbations on the governing equations are introduced to the RK3 time integration scheme by the acoustic time steps in order to increase the accuracy of the splitting method. These perturbed small acoustic time step equations are given below.

$$\partial_t U'' + (m_x/m_y)(\alpha^{t^*}/\alpha_d^{t^*}) \left[\mu_d^{t^*} \left(\alpha_d^{t^*} \partial_x p''^{\tau} + \alpha_d''^{\tau} \partial_x \bar{p} + \partial_x \phi''^{\tau} \right) + \partial_x \phi^{t^*} \left(\partial_\eta p'' - \mu_d'' \right)^{\tau} \right] = R_U^{t^*} \quad (33)$$

$$\partial_t V'' + (m_y/m_x)(\alpha^{t^*}/\alpha_d^{t^*}) \left[\mu_d^{t^*} \left(\alpha_d^{t^*} \partial_y p''^{\tau} + \alpha_d''^{\tau} \partial_y \bar{p} + \partial_y \phi''^{\tau} \right) + \partial_y \phi^{t^*} \left(\partial_\eta p'' - \mu_d'' \right)^{\tau} \right] = R_V^{t^*} \quad (34)$$

$$\delta_\tau \mu_d'' + m_x m_y [\partial_x U'' + \partial_y V'']^{\tau+\Delta\tau} + m_y \partial_\eta \Omega''^{\tau+\Delta\tau} = R_{\mu}^{t^*} \quad (35)$$

$$\delta_\tau \Theta_m'' + m_x m_y [\partial_x (U'' \theta_m^{t^*}) + \partial_y (V'' \theta_m^{t^*})]^{\tau+\Delta\tau} + m_y \partial_\eta (\Omega''^{\tau+\Delta\tau} \theta_m^{t^*}) = R_{\Theta}^{t^*} \quad (36)$$

$$\delta_\tau W'' - m_y^{-1} \mathbf{g} \left\{ (\alpha/\alpha_d)^{t^*} \left[\partial_\eta (C \partial_\eta \phi'') + \partial_\eta \left(\frac{c_s^2}{\alpha^{t^*}} \frac{\Theta_m''}{\Theta_m^{t^*}} \right) \right] - \mu_d'' \right\}^{\tau} = R_W^{t^*} \quad (37)$$

$$\delta_\tau \phi'' + \frac{1}{\mu_d^{t^*}} [m_y \Omega''^{\tau+\Delta\tau} \delta_\eta \phi^{t^*} - m_y \overline{gW''^{\tau}}] = R_\phi^{t^*}. \quad (38)$$

The full-time-split integration scheme (RK3 plus acoustic integration) is made of two nested loops: one outer loop for the RK3 integration and one inner loop for small-step acoustic mode integration. In the outer loop, physical parameterizations can be integrated either within the RK3 loop or externally using additive time-splitting. Furthermore, a single acoustic time step is used to put the solution forward time steps within the acoustic integration (Wicker & Skamarock, 2002). The significance of this time-splitting is that the time-splitting algorithm leads to a reduction in the number of these time-consuming processes by circumventing them because the computationally most expensive calculations are only performed in the RK3 steps, wherein the time step, Δt , associated with the RK3 time-splitting integration is dramatically larger than the acoustic time step, $\Delta\tau$.

Spatial discretization The variables used in the ARW solver are discretized in space on Arakawa-C grid shown in Fig. 29. While velocity components are staggered on their respective box faces, the prognostic scalar variables are defined at the center of the grid box (known as the mass points). Variable locations are indicated by the variable indices, i.e., $(x, y, \eta) = (i\Delta x, j\Delta y, k\Delta\eta)$. Since the ARW core uses a horizontally uniform grid, the horizontal grid spacings ($\Delta x, \Delta y$) are constant, however, the vertical grid spacing ($\Delta\eta$) is not fixed so that it can be specified by the user while setting-up the domain properties. This vertical stretching possibility is very important for such engineering applications as wind turbine parameterizations since wind turbines operate at the very bottom of the atmospheric boundary layer and are highly affected by vertical grid resolutions.

No averaging or interpolation effort is needed when coupling the vertical velocity to the column mass since it is staggered only in the vertical direction, however, new variables of the horizontal velocities should be defined as they are horizontally staggered relative to the column mass (Skamarock & Klemp, 2008). The discrete representation of the continuous variables, U, V , are and denoting \bar{a}^x as a linear interpolation operator:

$$U = \frac{\mu_d U}{m_y} \rightarrow \frac{\bar{\mu}_d^x U}{\bar{m}_y^x}, \quad V = \frac{\mu_d V}{m_x} \rightarrow \frac{\bar{\mu}_d^y V}{\bar{m}_x^y}.$$

Due to horizontal homogeneity of the ARW grid, the aforementioned operator turns into $\bar{a}^x = (a_{i+1/2} + a_{i-1/2})/2$. In light of these definitions, the spatially discrete acoustic step equations can be written

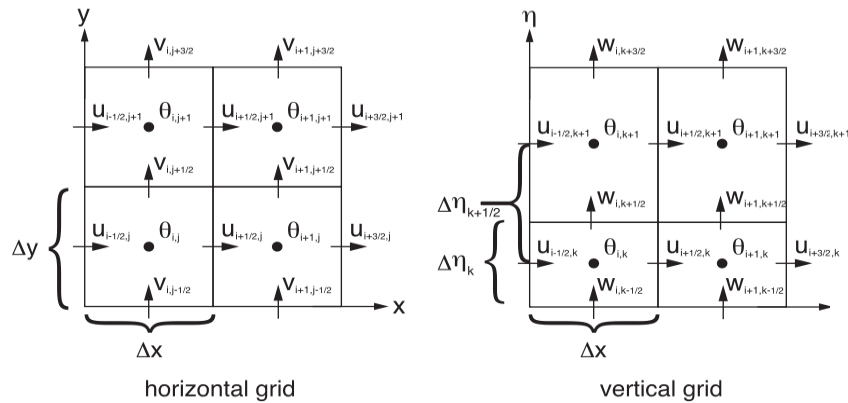


Figure 29: Horizontal and vertical grids of the ARW. Source: (Skamarock et al., 2019).

as:

$$\partial_t U'' + (m_x/m_y)(\alpha^{t^*}/\alpha_d^{t^*})^x \left[\mu_d^{t^*x} \left(\alpha_d^{t^*x} \partial_x p''\tau + \overline{\alpha_d''\tau^x} \partial_x \bar{p} + \partial_x \overline{\phi''\tau^\eta} \right) + \partial_x \overline{\phi^{t^*x\eta}} \left(\partial_\eta \overline{p''\tau^\eta} - \overline{\mu_d''^x} \right)^\tau \right] = R_U^{t^*} \quad (39)$$

$$\partial_t V'' + (m_y/m_x)(\alpha^{t^*}/\alpha_d^{t^*})^y \left[\mu_d^{t^*y} \left(\alpha_d^{t^*y} \partial_y p''\tau + \overline{\alpha_d''\tau^y} \partial_y \bar{p} + \partial_y \overline{\phi''\tau^\eta} \right) + \partial_y \overline{\phi^{t^*y\eta}} \left(\partial_\eta \overline{p''\tau^\eta} - \overline{\mu_d''^y} \right)^\tau \right] = R_V^{t^*} \quad (40)$$

$$\delta_\tau \mu_d'' + m_x m_y [\delta_x U'' + \delta_y V'']^{\tau+\Delta\tau} + m_y \delta_\eta \Omega''\tau + \Delta\tau = R_\mu^{t^*} \quad (41)$$

$$\delta_\tau \Theta_m'' + m_x m_y [\delta_x (U'' \overline{\theta_m^{t^*x}}) + \delta_y (V'' \overline{\theta_m^{t^*y}})]^{\tau+\Delta\tau} + m_y \delta_\eta (\Omega''\tau + \Delta\tau \overline{\theta_m^{t^*\eta}}) = R_{\Theta_m}^{t^*} \quad (42)$$

$$\delta_\tau W'' - m_y^{-1} g \left\{ (\alpha/\alpha_d)^{t^*x\eta} \left[\delta_\eta (C \delta_\eta \phi'') + \delta_\eta \left(\frac{c_s^2}{\alpha^{t^*}} \frac{\Theta_m''}{\Theta_m^{t^*}} \right) \right] - \mu_d'' \right\}^\tau = R_W^{t^*} \quad (43)$$

$$\delta_\tau \phi'' + \frac{1}{\mu_d^{t^*}} [m_y \Omega''\tau + \Delta\tau \delta_\eta \overline{\phi^{t^*x\eta}} - m_y g \overline{W''\tau}] = R_\phi^{t^*}, \quad (44)$$

where the discrete operator is

$$\delta_x a = \Delta x^{-1} (a_{i+1/2} - a_{i-1/2}). \quad (45)$$

The variables on mass levels (k) are vertically interpolated to the (w) levels ($k + \frac{1}{2}$) (Skamarock et al., 2019).

5.2.5 Physical parameterizations

The atmospheric processes (e.g., microphysics, cumulus, PBL, land-surface interaction, and radiation) are parameterized within the WRF physics package, including plenty of choices. The interaction between physics in the ARW core is sketched in Fig. 30. The dynamics and physics solvers in the ARW core are separated from each other since the physics solver uses its own drivers to call their routines to be handled in the dynamics solver. These drivers bridge the gap between the dynamics and physics solver utilizing a pre-physics preparation algorithm as well as post-physics manipulations of the tendencies (Wang et al., n.d.), (S.-H. Chen & Dudhia, n.d.).

Physics packages in the ARW core compute the un-staggered velocity tendencies, potential temperature, and moisture fields that are previously processed by the pre-physics routines, and then the information gathered by these routines is fed into a post-physics step that re-staggers fundamental tendencies, couples with coordinate metrics and sends them to the dynamics solver. One has to be stressed that each physics scheme has to be initialized within the pre-physics step. This initialization part may be

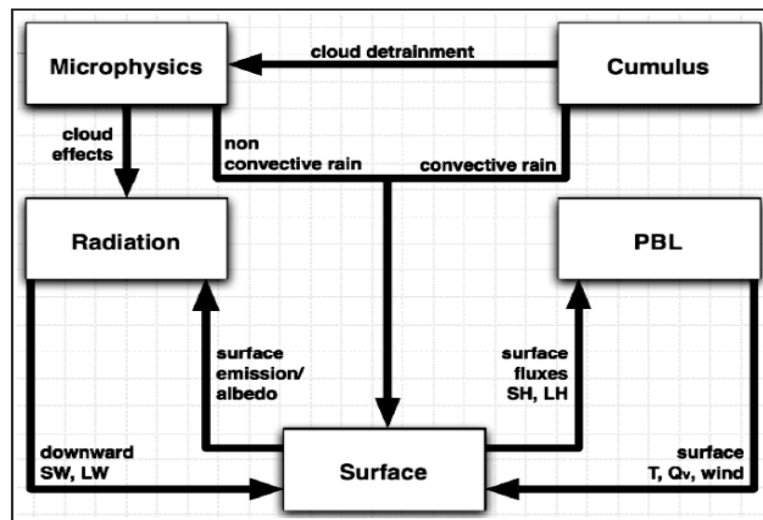


Figure 30: Interactions among various physical parameterization schemes. Taken from: (Dudhia, 2014).

very important for those schemes which require reading external data or calculation of look-up tables of functions (Skamarock et al., 2019). Therefore, each physical parameterization routine should include its own initialization routine and should be called via common or their own physics drivers. Apart from that, from wind modeling point of view, the planetary boundary layer (PBL) parameterizations are the most significant.

PBL parameterization A planetary boundary layer (PBL) scheme is designed to picture all the characteristics of the ABL regions as well as the diurnally changing stability regimes and distribute surface and boundary layer eddy fluxes to extend PBL in depth. It also calculates vertical fluxes not only within the ABL but also across the whole atmospheric column. On the contrary, the horizontal diffusion is computed with respect to the horizontal deformation (Skamarock et al., 2019). Although surface fluxes are provided by common surface layer and land-surface schemes, some PBL models ask for their own land-surface schemes, e.g., Mellor–Yamada Nakanishi Niino (MYNN) (Nakanishi & Niino, 2006), (Nakanishi & Niino, 2009), Quasi–normal Scale Elimination (QNSE) (Sukoriansky, Galperin, & Perov, 2005), Mellor–Yamada–Janjic (MYJ) (Janjic, 1994) schemes. The PBL schemes are one-dimensional and are based on the assumption of scale-separation between energy-containing eddies and subfilter ones, creating a buffer zone (called as gray zone, see section 5.3.1) lies between these two scales. Many of the PBL schemes are based on dry mixing, yet the saturation effects can also be involved in the vertical stability, which has effects on the mixing (Skamarock et al., 2019).

Over the years, a number of PBL schemes have been proposed and have been implemented into WRF such as Yonsei University Scheme (YSU) (Hong, Noh, & Dudhia, 2006), Mellor–Yamada–Janjic Scheme (MYJ) (Janjic, 1994), Quasi–normal Scale Elimination (QNSE) Scheme (Sukoriansky et al., 2005), Mellor–Yamada Nakanishi Niino (MYNN) Level 2.5 (Nakanishi & Niino, 2006) and Level 3 (Nakanishi & Niino, 2009) Schemes, Asymmetric Convection Model 2 Scheme (ACM2) (Pleim, 2007), Bougeault–Lacarrere Scheme (BouLac) (Bougeault & Lacarrere, 1989), Shin-Hong Scale–aware Scheme (Shin & Hong, 2015), and MRF Scheme (Hong & Pan, 1996). Recently, a 3D scale-adaptive turbulent kinetic energy scheme by Zhang et al. (X. Zhang, Bao, Chen, & Grell, 2018a), a new PBL scheme based on LES, VKI01, by Senel et al. (Senel, Temel, Porchetta, Munoz-Esparza, & van Beeck, 2019), and (X. Zhang, Bao, Chen, & Grell, 2018b) have also been proposed.

5.3 WRF-LES

As mentioned in the earlier sections, the WRF code has the capability of performing ideal and real case simulations. The ideal case simulations do not involve any coupling to mesoscale simulations or do not require real-world meteorological forcing on the inflow boundaries while real cases do need these forcing inputs. Moreover, idealized simulations are conducted in a horizontally periodic flow domain using homogeneous and steady inflow conditions. Numerous input variables and physical properties of the flow domain play important role on the resultant real case simulation, e.g., the surface boundary conditions, meteorological forcing data, and the land-surface model used by the PBL schemes (Talbot, Bou-Zeid, & Smith, 2012). In both ideal and real case scenarios, WRF-LES is preferable for horizontal grid resolutions up to about 100 m, and running WRF in LES mode triggers turbulence three-dimensionally and utilizes distinct vertical and horizontal diffusion schemes unlike 1D PBL schemes (C. Moeng, Dudhia, Klemp, & Sullivan, 2007). In other words, all major eddies are resolved by 3D turbulence schemes, and small-sized ones are filtered out. Bryan (Bryan, 2012) suggested that the LES-SFS closure schemes are not beneficial at mesoscale grid sizes (grid sizes order of 1 km) because they are developed for grid sizes that fall in the inertial subrange. Latest version of the Advanced Research WRF (ARW-WRF) contains three SFS models. The simplest is the Smagorinsky model (Smagorinsky, 1963), (Lilly, 1967), more advanced to the Smagorinsky model being the 1.5-order SFS TKE (Lilly, 1967), and the nonlinear backscatter and anisotropy (NBA) model (Kosovic, 1997). The eddy-viscosity coefficients, ν_t , of the Smagorinsky and 1.5-order TKE models are

$$\nu_t = (C_s \Delta)^2 \max[0, (\tilde{S}_{ij} \tilde{S}_{ij} - Pr^{-1} N^2)^{1/2}]; \quad (46)$$

where C_s is the Smagorinsky coefficient, which in WRF it is 0.18 by default. Δ is the subfilter size, $Pr = 0.7$ is the Prandtl number, and N^2 is the Brunt-Vaisala frequency.

$$\nu_t = C_k \ell \sqrt{k}, \quad (47)$$

where k is the SFS turbulent kinetic energy, and $C_k = 0.15$. Also, there is an additional prognostic SFS TKE equation that is solved when the 1.5-order SFS TKE scheme is activated.

These two SFS closure schemes are based on the eddy-viscosity approach, formulated in Eq. ??, while the NBA model takes into account the backscattering and anisotropy. Moreover, the Smagorinsky and 1.5-order TKE models assume the local balance between turbulence dissipation and production. This assumption is not appropriate while conducting simulations over complex terrain as the topographical features and surface roughness are heterogeneous (Lundquist & Chan, 2007). Furthermore, backscatter was not taken into account, and these eddy-viscosity-based SFS closure models relate the SFS stresses linearly to the strain stresses, failing to accurately predict the SFS stresses (J. D. Mirocha, Lundquist, & Kosovic, 2010). The NBA model stress is expressed in terms of SFS TKE as:

$$M_{ij} = -C_k \Delta \left\{ 2(k)^{1/2} \tilde{S}_{ij} + \left(\frac{27}{8\pi}\right)^{1/3} C_s^{2/3} \Delta \left[C_1 \left(\tilde{S}_{ik} \tilde{S}_{kj} - \frac{1}{3} \tilde{S}_{mn} \tilde{S}_{mn} \delta_{ij} \right) + C_2 \left(\tilde{S}_{ik} \tilde{R}_{kj} - \tilde{R}_{ik} \tilde{S}_{kj} \right) \right] \right\}; \quad (48)$$

where the resolved rotation rate tensor is formulated as $\tilde{R}_{ij} = (1/2)(\partial \tilde{u}_i / \partial x_j - \partial \tilde{u}_j / \partial x_i)$, $C_s = [8(1 + C_b)/27\pi^2]^{1/2}$, $C_e = (8\pi/27)^{1/3} C_s^{4/3}$, $C_1 = C_2 = 960^{1/2} C_b / 7(1 + C_b) S_k$, $S_k = 0.5$, and $C_b = 0.36$ (J. D. Mirocha et al., 2010). Some dynamic subfilter-scale stress models for LES by Kirkil et al. (Kirkil, Mirocha, Chow, & Kosovic, 2011) have also been implemented into WRF, but these models are not publicly available in the latest version of the WRF code.

5.3.1 Terra-incognita

Over the past years, many scientists have worked on the coupling of mesoscale and microscale simulations across scales. There have been two ways of coupling these separate scales defined in the literature, e.g., performing mesoscale simulations without coupling with microscale and projecting this mesoscale flow to a solver, which has a finer-resolution domain, as the initial and boundary conditions of

the LES mode. The other way of handling this transition is the direct and full coupling of mesoscale and microscale within a specific solver (Doubrawa, Montornes, Barthelmie, Pryor, & Casso, 2018). Such coupling generally lies between a wide range of spatial scales.

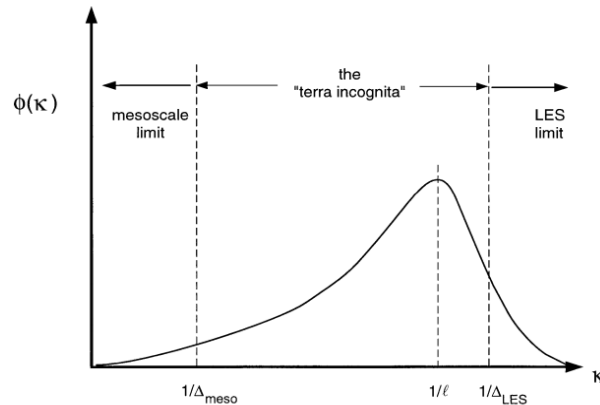


Figure 31: Sketch of the energy spectrum $\phi(\kappa)$ in the horizontal plane where κ is wavenumber. Source: (Wyngaard, 2004).

According to Wyngaard (Wyngaard, 2004), turbulence parameterization schemes, either 1D or 3D schemes, can not accurately simulate turbulence in both mesoscale and microscale simulations, and thus this specified range of spatial scales (generally between ~ 100 m and ~ 1000 m grid spacing) in which existing turbulence closure schemes are expected to fail was named as the *terra incognita* or *gray zone* (Fig.31). These grid spacing at the lower and upper boundaries of the terra incognita are not constant, and according to Rai et al. (Rai et al., 2019), the upper limit of the gray zone can be stretched based on the depth of the PBL. Moreover, if the horizontal grid spacing is less than the ABL depth, artificial roles appear in the mesoscale-microscale coupling, whereas they do not exit when Δ_{xy} is greater than or at the depth of the boundary layer. Also, microscale results are not affected by the coupled mesoscale domains when their grid sizes fall into the terra incognita, as found in the study of Rai et al. (Rai et al., 2019).

The major difference between mesoscale and microscale is the value of ℓ/Δ , the ratio between the energy-containing turbulence scale and the scale of the spatial filter (Wyngaard, 2004). In LES mode, this ratio is large. Therefore, the energy-containing turbulence is resolved, while in RANS mode, turbulence is parameterized in mesoscale, so turbulence is not resolved as the ratio of ℓ/Δ is small. Wyngaard (Wyngaard, 2004) has pointed out that the only key point determining the eddy viscosity is the length scale considering the turbulent closures in mesoscale and microscale simulations. This length scale, ℓ , is directly associated with the spatial grid size in the LES, while the largest scale (i.e., the integral scale) across the whole boundary layer defines the length scale in the RANS simulations. To sum up, a theoretical approach for the transition of the length scale from RANS to LES mode based on the model resolution is required in addition to the TKE-based prognostic formulations.

5.3.2 Scale-adaptive 3D PBL schemes

In recent years, the LES turbulence closures have been extensively investigated and altered by adding scale adaptivity to them to parameterize the terra incognita, which is described above in detail. A mixing length scale based on a scale-adaptive formulation has been proposed by Kurowski and Teixeira (Kurowski & Teixeira, 2018). This mixing length scale increases gradually till the boundary layer length scale. Kitamura (Kitamura, 2016) modified the length scale formulation in a TKE closure considering the anisotropic turbulence in the terra incognita. Although the use of a modified length scale is a relatively simple approach, formulations based on the altered or simplified prognostic equations of turbulence closure models have also been studied for the terra incognita. Most of the studies by Wyngaard

(Wyngaard, 2004), Hatlee and Wyngaard (Hatlee & Wyngaard, 2007), and Ramachandran and Wyngaard (Ramachandran & Wyngaard, 2011) have reported that such TKE-based models perform better than simple eddy-diffusivity models, yet bring about more computational cost as the prognostic equations are integrated for all SFS fluxes. Some PBL schemes being used have also been further extended to account for the terra incognita parameterization. To do so, Zhou et al. (Zhou, Zhu, & Xue, 2017) have associated the horizontal eddy diffusivity with the characteristic length of the unstable boundary layer and have developed a new formulation for horizontal mixing in the CBL. Ito et al. (Ito, Niino, Nakanishi, & Moeng, 2015) have also worked on the scale-adaptive schemes, and they have related the horizontal grid spacing to the length scales that dominate the CBL. They used the Mellor-Yamada PBL model (Nakanishi & Niino, 2009) in their studies. A set of functions based on explicit grid-spacing in a non-local PBL scheme have been prescribed by Shin and Hong (Shin & Hong, 2015). A blending parameter associated with the ratio between grid spacing and the boundary layer depth was used to blend a 1D PBL scheme to a 3D LES scheme by Boutle et al. (Boutle, Eyre, & Lock, 2014). Another effort was put into the extension of the eddy-diffusivity mass-flux (EDMF) scheme for the terra incognita by Siebasma et al. (Siebasma & Soares, 2007). Recently, a 3D scale-adaptive TKE scheme has been implemented in WRF by Zhang et al. (X. Zhang et al., 2018b). Although dry atmospheric conditions have generally been investigated by researchers for terra-incognita parameterization, a couple of studies on simulations of moist convection revealed that 1D PBL schemes predict turbulence worse than those 3D closure models (Fiori, Parodi, & Siccardi, 2010), (Machado & Chaboureau, 2015). Although terra-incognita parameterization schemes have widely been investigated, further validation studies and intercomparison studies of turbulence closures have to be done, especially for complex terrains (Chow et al., 2019).

6 Conclusions

The atmospheric boundary layer simulation technologies considering experimental and numerical approaches for atmospheric flows over flat and complex terrains as well as in urban areas are examined in this document. Characteristics of the planetary boundary layer (i.e., atmospheric boundary layer) under various atmospheric stability conditions are introduced in Chapter 1 before giving details of the atmospheric flows in Chapter 2. The various flow features encountered in flat terrains, complex terrains, and urban environments are introduced in Sections 2.1 - 2.3. ABL modeling in the wind tunnel is crucial for model validation under controlled conditions. The details of physics required to be modeled depend on the type of urban application such as pedestrian comfort, urban wind energy, or pollution dispersion. For urban wind energy, the regions of high-speed flow are of particular interest. In addition to the experimental techniques, computational methods for atmospheric flows are also important to simulate complex flows and are generally preferred to the experimental methods due to being cost-efficient and easier to perform. The state-of-the-art in multi-scale atmospheric flow simulations using the RANS/URANS and LES approaches are dealt with in Chapter 4. The proposed guidelines for simulations provide a useful starting point for the selection of parameters for accurate ABL modeling. A detailed review of Numerical Weather Prediction (NWP) modeling is presented in Chapter 5. The use of precise turbulent inflow conditions for wind energy applications has importance for accurately predicting turbulence statistics. This is done using real-time forcing turbulent inflow conditions stored in the re-analyses dataset. These inputs are utilized by the NWP models such as the Weather Research and Forecasting (WRF) model and the information coming from mesoscale is carried into microscale domains to perform high-fidelity simulations, for instance; Large Eddy Simulations (LES). Details for such simulations are given in Sections 5.1 - 5.3.

7 Acknowledgments

This project has received funding from the European Union's Horizon 2020 research and innovation programme under grant agreement No EC grant 860101. We are grateful to that and the members who are not listed as co-authors for their helpful discussions and comments.

References

- Adcroft, A. J., Hill, C. N., & Marshall, J. C. (1999). A new treatment of the coriolis terms in c-grid models at both high and low resolutions. *Monthly Weather Review*, *127*(8).
- AmetSOC. (2012a). Retrieved from http://glossary.ametsoc.org/wiki/Atmospheric_boundary_layer (Accessed: 14.09.2020)
- AmetSOC. (2012b). Retrieved from http://glossary.ametsoc.org/wiki/Geostrophic_wind_level (Accessed: 14.09.2020)
- Andrews, D. G. (2010). *An introduction to atmospheric physics*. Cambridge University Press.
- Arnold, S. J., & ApSimon, H. (2004). Introduction to the dapple air pollution project. *Sci. Total Environ.*, *332* (1-3), 139-153.
- ASCE. (1999). Wind tunnel studies of buildings and structure: Manuals and reports on engineering practice 67 [Computer software manual].
- Basu, S. (2017). Mesoscale modeling of atmospheric flows for wind energy applications. In *Cfd for atmospheric flows and wind engineering*. Belgium: VKI Lecture Series.
- Bendjebbas, H., abdellah el hadj, A., & Abbas, M. (2016, 02). Full-scale, wind tunnel and cfd analysis methods of wind loads on heliostats: A review. *Renewable and Sustainable Energy Reviews*, *54*, 452–472. doi: 10.1016/j.rser.2015.10.031
- Blocken, B. (2019). *Introduction to the simulation of atmospheric flows* (Vol. 1). Belgium: von Karman Institute for Fluid Dynamics.
- Blocken, B., Carmeliet, J., & Stathopoulos, T. (2007). Cfd evaluation of wind speed conditions in passages between parallel buildings-effect of wall-function roughness modifications for the atmospheric boundary layer flow. *Journal of Wind Eng. Ind. Aerodynamics*, *95*, 9-11.
- Bosilovich, M. G., Kennedy, J., Dee, D., Allan, R., & O'Neill, A. (2013). On the reprocessing and reanalysis of observations for climate. In A. Ghassem & J. W. Hurrell (Eds.), *Climate science for serving society: Research, modeling and prediction priorities* (pp. 51–71). Springer.
- Bougeault, P., & Lacarrere, P. (1989). Parameterization of orography-induced turbulence in a meso-beta-scale model. *Mon. Wea. Rev.*, *117*, 1872–1890.
- Boutle, I., Eyre, J., & Lock, A. (2014). Seamless stratocumulus simulation across the turbulent gray zone. *Mon. Weather Rev.*, *142*, 1655–1668.
- Bryan, G. H. (2012). Effects of surface exchange coefficients and turbulence length scales on the intensity and structure of numerically simulated hurricanes. *Mon. Wea. Rev.*, *140*, 1125–1140.
- Butler, D. K., & Dagneu, D. A. (2013). *Where the wild winds blow, part i*. <https://www.air-worldwide.com/publications/air-currents/2013/where-the-wild-winds-blow-part-i/>. (Accessed: 2020-09-30)
- Chandrasekar, A. (2010). *Basics of atmospheric science*. PHI Learning Private Limited.
- Chen, F., & Dudhia, J. (2001). Coupling an advanced land surface-hydrology model with the Penn State-NCAR MM5 modeling system. part i: Model implementation and sensitivity. *Mon. Weather Rev.*, *129*(4), 569–585.
- Chen, S.-H., & Dudhia, J. (n.d.). *Annual report: Wrf physics* (Tech. Rep.).
- Cho, M. (2010). The politics of urban nature restoration: the case of cheonggye- cheon restoration in seoul, korea. *Int Dev Plan Rev.*, *18*, 145-65.

- Chou, C., Lee, C., Chen, W., Chang, S., Chen, T.-K., & Lin, C.-Y. (2007). Lidar observations of the diurnal variations in the depth of urban mixing layer: a case study on the air quality deterioration in taipei,taiwan. *Sci Total Environ.*, 374, 156-66.
- Chow, F. K., Schar, C., Ban, N., Lundquist, A., K., Schlemmer, L., & Shi, X. (2019). Crossing multiple gray zones in the transition from mesoscale to microscale simulation over complex terrain. *Atmosphere*, 10(2), 1–38.
- Deodatis, G., & Shinozuka, M. (1988). Auto-regressive model for nonstationary stochastic processes. *Journal of engineering mechanics*, 114(11), 1995–2012.
- Doubrawa, P., Montornes, A., Barthelmie, R. J., Pryor, S. C., & Casso, P. (2018). Analysis of different gray zone treatments in wrf-les real case simulations. *Wind Energ. Sci. Discuss.*
- Dudhia, J. (2014). A history of mesoscale model development. *J. Atmos. Sci.*, 50(1), 121–131.
- Emeis, S. (2018). *Wind energy meteorology* (Vol. 2). Belgium: Springer International Publishing.
- Faken, T. (2017). *Micrometeorology*. Springer.
- Fernando, H., Mann, J., Laginha Palma, J., & Lundquist, J. (2018, 11). The perdigão: Peering into microscale details of mountain winds. *Bulletin of the American Meteorological Society*. doi: 10.1175/BAMS-D-17-0227.1
- Fernando, H. J. S., Mann, J., Palma, J. M. L. M., Lundquist, J. K., Barthelmie, R. J., Belo-Pereira, M., ... Wang, Y. (2019). The Perdigão: Peering into Microscale Details of Mountain Winds. *Bulletin of the American Meteorological Society*, 100(5), 799 - 819. Retrieved 09-01-2023, from <https://journals.ametsoc.org/view/journals/bams/100/5/bams-d-17-0227.1.xml> doi: 10.1175/BAMS-D-17-0227.1
- Finardi, S., Morselli, M. G., & P., J. (1989). *Wind flow models over complex terrain for dispersion calculations* (Tech. Rep.). Riso National Laboratory, Roskilde, Denmark.
- Fiori, E., Parodi, A., & Siccardi, F. (2010). Turbulence closure parameterization and grid spacing effects in simulated supercell storms. *J. Atmos. Sci.*, 67, 3870–3890.
- Floater, M. S., & Hormann, K. (2014). *Surface parameterization: a tutorial and survey*.
- Franke, J., & Baklanov, A. (2007). *Best practice guideline for the cfd simulation of flows in the urban environment: Cost action 732 quality assurance and improvement of microscale meteorological models*.
- Garratt, J. R. (1992). *The atmospheric boundary layer*. Cambridge University Press.
- Geiger, R., Aron, R. H., & Todhunter, P. (1995). *The climate near the ground*. Cambridge University Press.
- Grigoriu, M. (2002). *Stochastic calculus: Applications in science and engineering* (Vol. 1st edition) (Nos. 04; QA280, P7.). Birkhäuser Basel.
- Gryning, S. E., Batchvarova, E., Brümmner, B., Jorgensen, H., & Larsen, S. (2007). On the extension of the wind profile over homogeneous terrain beyond the surface boundary layer. *Boundary-Layer Meteorology*, 251–268.
- Hågbo, T.-O., & Giljarhus, K. E. T. (2022). Pedestrian wind comfort assessment using CFD simulations with varying number of wind directions. *Frontiers in Built Environment*, 8, 110. doi: <https://doi.org/10.3389/fbuil.2022.858067>
- Hågbo, T.-O., Giljarhus, K. E. T., & Hjertager, B. H. (2021). Influence of geometry acquisition method on pedestrian wind simulations. *Journal of Wind Engineering and Industrial Aerodynamics*, 215, 104665. doi: <https://doi.org/10.1016/j.jweia.2021.104665>
- Haltiner, G. J., & Williams, R. T. (1980). *Numerical prediction and dynamic meteorology*. John Wiley and Sons, Inc.

- Hatlee, S. C., & Wyngaard, J. C. (2007). Improved subfilter-scale models from the hats field data. *JJ. Atmos. Sci.*, *64*, 1694–1705.
- Holton, R. J., & Hakim, G. J. (2013). *An introduction to dynamic meteorology*. Elsevier.
- Hong, S., Noh, Y., & Dudhia, J. (2006). A new vertical diffusion package with an explicit treatment of entrainment processes. *Mon. Wea. Rev.*, *134*, 2318–2341.
- Hong, S., & Pan, H. (1996). Nonlocal boundary layer vertical diffusion in a medium–range forecast model. *Mon. Wea. Rev.*, *124*, 2322–2339.
- Iacono, M., Delamere, J., Mlawer, E., Shephard, M., Clough, S., & Collins, W. (2008). Radiative forcing by long-lived greenhouse gases: Calculations with the AER radiative transfer models. *Journal of Geophysical Research: Atmospheres*, *113*(D13). doi: <https://doi.org/10.1029/2008JD009944>
- Ito, J., Niino, H., Nakanishi, M., & Moeng, C.-H. (2015). An extension of the mellor–yamada model to the terra incognita zone for dry convective mixed layers in the free convection regime. *Boundary-Layer Meteorology*, *157*(1), 23–43.
- Janjic, Z. I. (1994). The step–mountain eta coordinate model: Further developments of the convection, viscous sublayer, and turbulence closure schemes. *Mon. Wea. Rev.*, *122*, 927–945.
- Janssen, W., Blocken, B., & van Hooff, T. (2012). Pedestrian wind comfort around buildings: comparison of wind comfort criteria based on whole-flow field data for a complex case study. *Build Environ.*
- Jiménez, P., Dudhia, J., González-Rouco, J., Navarro, J., Montávez, J., & García-Bustamante, E. (2012). A revised scheme for the WRF surface layer formulation. *Monthly weather review*, *140*(3), 898–918.
- Kaimal, J. C., & Finnigan, J. J. (1994). *Atmospheric boundary layer flows: Their structure and measurement*. Oxford University Press.
- Kain, J. (2004). The Kain–Fritsch convective parameterization: an update. *Journal of applied meteorology*, *43*(1), 170–181.
- Kale, B. (2023). *ABL simulations with uncertain weather parameters and impact on WT performance and near-field noise* (PhD dissertation). Universidad Politécnica de Madrid.
- Kim, J.-J., & Baik, J.-J. (2003). A wind-tunnel study of turbulent flow close to regularly arrayed rough surfaces. *Journal of Wind Eng Ind Aero dyn.*, *91*, 309–29.
- Kirkil, G., Mirocha, J. D., Chow, F. K., & Kosovic, B. (2011). Implementation and evaluation of dynamic subfilter-scale stress models for large-eddy simulation using wrf*. *Mon. Wea. Rev.*, *140*, 266–284.
- Kitamura, Y. (2016). Improving a turbulence scheme for the terra incognita in a dry convective boundary layer. *J. Meteorol. Soc. Jpn. Ser. II*, *94*, 491–506.
- Kleinhans, D., Friedrich, R., Schaffarczyk, A., & Peinke, J. (2009). Synthetic turbulence models for wind turbine applications. In *Progress in turbulence iii* (pp. 111–114). Springer.
- Klemp, J. B., Skamarock, W. C., & Dudhia, J. (2007). Conservative split-explicit time integration methods for the compressible nonhydrostatic equations. *Mon. Wea. Rev.*, *135*, 2897–2913.
- Klemp, J. B., & Wilhelmson, R. (1978). The simulation of three-dimensional convective storm dynamics. *J. Atmos. Sci.*, *35*, 1070–1096.
- Kosovic, B. (1997). Subgrid-scale modelling for the large-eddy simulation of high-reynolds-number boundary layers. *J. Fluid Mech.*, *336*, 151–182.
- Krenk, S., & Møller, R. N. (2019). Turbulent wind field representation and conditional mean-field simulation. *Proceedings of the Royal Society A*, *475*(2223), 20180887.
- Kurowski, M., & Teixeira, J. (2018). A scale-adaptive turbulent kinetic energy closure for the dry convective boundary layer. *J. Atmos. Sci.*, *75*, 675–690.

- Laginha Palma, J., Silva, C., Costa Gomes, V., Lopes, A., Esteves, T., & Batista, V. (2020, 11). The digital terrain model in the computational modelling of the flow over the Perdigão site: the appropriate grid size. *Wind Energy Science*, 5, 1469-1485. doi: 10.5194/wes-5-1469-2020
- Laprise, R. (1992). The euler equations of motion with hydrostatic pressure as an independent variable. *Monthly Weather Review*, 120, 197–207.
- Leloudas, G. (2006). *Optimization of wind turbines with respect to noise* (MSc thesis). Technical University of Denmark.
- Lettau, H. (1969). Note on aerodynamic roughness-parameter estimation on the basis of roughness-element description. *Journal of Appl Meteorol.*, 8, 828-32.
- Ligda, M. G. H. (1951). Radar storm observation. *Compendium of Meteorology*.
- Lilly, D. K. (1967). The representation of small-scale turbulence in numerical experiment. *Proc. IBM Scientific Computing Symp. on Environmental Sciences*.
- Liu, Z., Liu, Z., & Peng, Y. (2017). Dimension reduction of karhunen-loeve expansion for simulation of stochastic processes. *Journal of Sound and Vibration*, 408, 168–189.
- Lundquist, J. K., & Chan, S. T. (2007). Consequences of urban stability conditions for computational fluid dynamics simulations of urban dispersion. *J. Appl. Meteor. Climatol.*, 46, 1080–1097.
- M, R., Thom, A., & Edwards, I. (1980). A wind-tunnel study of turbulent flow close to regularly arrayed rough surfaces. *Bound-LayerMeteorol.*, 18, 373-97.
- Machado, L. A., & Chaboureau, J. P. (2015). Effect of turbulence parameterization on assessment of cloud organization. *Mon. Weather Rev.*, 143, 3246–3262.
- McGuffie, K., & Henderson-Sellers, A. (1997). *A climate modelling primer*. John Wiley and Sons.
- Mignolet, M. P., & Spanos, P. D. (1992). Simulation of homogeneous two-dimensional random fields: Part i—ar and arma models.
- Mirocha, J., Kosovic, B., & Kirkil, G. (2014). Resolved turbulence characteristics in large-eddy simulations nested within mesoscale simulations using the weather research and forecasting model. *Monthly Weather Review*, 142, 806–831.
- Mirocha, J. D., Lundquist, J. K., & Kosovic, B. (2010). Implementation of a nonlinear subfilter turbulence stress model for large-eddy simulation in the advanced research wrf model. *Mon. Wea. Rev.*, 138, 4212–4228.
- Moeng, C., Dudhia, J., Klemp, J., & Sullivan, P. (2007). Examining the two-way grid nesting for large-eddy simulation of the pbl using the wrf model. *Mon. Wea. Rev.*, 135, 2295–2311.
- Moeng, C. H. (2016, June). Lecture notes on the planetary boundary layer [Computer software manual].
- Monahan, J. F. (2011). *Numerical methods of statistics*. Cambridge University Press.
- Munoz-Esparza, D. (2017). Generation of resolved atmospheric boundary layer turbulence in coupled mesoscale-to-les models using a stochastic temperature perturbation method. In *Cfd for atmospheric flows and wind engineering*. Belgium: VKI Lecture Series.
- Munoz-Esparza, D., Kosovic, B., Mirocha, J., & van Beeck, J. (2014). Bridging the transition from mesoscale to microscale turbulence in numerical weather prediction models. *Boundary-Layer Meteorology*, 153, 409–440.
- Munoz-Esparza, D., Kosovic, B., van Beeck, J., & Mirocha, J. (2015). A stochastic perturbation method to generate inflow turbulence in large-eddy simulation models: Application to neutrally stratified atmospheric boundary layers. *Physics of Fluids*, 27.

- Nakanishi, M., & Niino, H. (2006). An improved Mellor–Yamada level 3 model: its numerical stability and application to a regional prediction of advecting fog. *Bound.-Layer Meteor.*, *119*, 397–407.
- Nakanishi, M., & Niino, H. (2009). Development of an improved turbulence closure model for the atmospheric boundary layer. *J. Meteor. Soc.*, *87*, 895–912.
- Ng, E., Yuan, C., & Chen, L. (2011). Improving the wind environment in high-density cities by understanding urban morphology and surface roughness: a study in Hong Kong. *Landsc Urban Plan.*, *101*, 59–74.
- Oke, T. (2004). Initial guidance to obtain representative meteorological observations at urban sites. *World Meteorological Organization Geneva*, *81*.
- Oke, T. R. (1987). *Boundary layer climates*. Taylor and Francis.
- Orgill, M. M. (1981). *Atmospheric studies in complex terrain: A planning guide for future studies* (Tech. Rep.). Pacific Northwest Laboratory, Richland, Washington.
- Park, M., Hagishima, A., Tanimoto, J., & Narita, K. I. (2012). Effect of urban vegetation on outdoor thermal environment: field measurement at a scale model site. *Build. Environ.*, *56*, 38–46.
- Park, S.-H., Skamarock, W., Klemp, J., Fowler, L., & Duda, M. (2013). Evaluation of global atmospheric solvers using extensions of the Jablonowski and Williamson baroclinic wave test case. *Monthly Weather Review*, *141*, 3116–3129.
- Parker, W. S. (2016). Reanalyses and observations - what's the difference? *American Meteorological Society*.
- Peña, A., Floors, R., Sathe, A., Gryning, S.-E., Wagner, R., Courtney, M., ... Hasager, C. (2016). Ten years of boundary-layer and wind-power meteorology at Høvsøre, Denmark. *Boundary-Layer Meteorology*, *158*, 1–26.
- Pielke, R. A. (2013). *Mesoscale meteorological modeling*. Elsevier.
- Plate, E. J., & Cermak, J. E. (1963). *Micrometeorological wind tunnel facility, description and characteristics*.
- Pleim, J. E. (2007). A combined local and nonlocal closure model for the atmospheric boundary layer. part I: Model description and testing. *J. Appl. Meteor. Climatol.*, *46*, 1383–1395.
- Rai, R. K., Berg, L. K., Kosovic, B., Haupt, S. E., Mirocha, J. D., Ennis, B. L., & Draxl, C. (2019). Evaluation of the impact of horizontal grid spacing in terra incognita on coupled mesoscale–microscale simulations using the WRF framework. *Monthly Weather Review*, *147*, 1007–1027.
- Ramachandran, S., & Wyngaard, J. C. (2011). Subfilter-scale modelling using transport equations: Large-eddy simulation of the moderately convective atmospheric boundary layer. *Bound.-Layer Meteorol.*, *139*, 1–35.
- Raupach, M., Thom, A., & Edwards, I. (1980). A wind-tunnel study of turbulent flow close to regularly arrayed rough surfaces. *Bound.-Layer Meteorol.*, *18*, 373–97.
- Razak, A., Hagishima, A., Ikegaya, N., & Tanimoto, J. (2012). Analysis of airflow over building arrays for assessment of urban wind environment. *Build Environ*, 373–97.
- Ringler, D. T., Heikes, R. P., & Randall, D. A. (2000). Modeling the atmospheric general circulation using a spherical geodesic grid: A new class of dynamical cores. *American Meteorological Society*, *128*, 2471–2490.
- Salizzoni, P., & Van Liefferinge, R. (2009). Influence of wall roughness on the dispersion of a passive scalar in a turbulent boundary layer. *Atmos Environ*, *43*, 734–48.
- Schmidt, J., Peralta, C., & Stoevesandt, B. (2012, 10). Automated generation of structured meshes for wind energy applications..

- Senel, C. B., Temel, O., Porchetta, S., Munoz-Esparza, D., & van Beeck, J. (2019). A new planetary boundary layer scheme based on les: Application to the xpia campaign. *Journal of Advances in Modeling Earth Systems*, 2655–2679.
- Shin, H. H., & Hong, S.-Y. (2015). Representation of the subgrid-scale turbulent transport in convective boundary layers at gray-zone resolutions. *Mon. Wea. Rev.*, 143, 250–271.
- Shinozuka, M., & Jan, C.-M. (1972). Digital simulation of random processes and its applications. *Journal of sound and vibration*, 25(1), 111–128.
- Siebesma, A. P., & Soares, J., P. M. and Teixeira. (2007). A combined eddy-diffusivity mass-flux approach for the convective boundary layer. *J. Atmos. Sci.*, 64, 1230–1248.
- Skamarock, W. C., & Klemp, J. B. (2008). A time-split nonhydrostatic atmospheric model for weather research and forecasting applications. *Journal of Computational Physics*, 227, 3465–3485.
- Skamarock, W. C., Klemp, J. B., Dudhia, J., Gill, D. O., Liu, Z., Berner, J., . . . Huang, X.-Y. (2019). *Description of the advanced research wrf model version 4* (Tech. Rep.). NCAR.
- Smagorinsky, J. (1963). General circulation experiments with the primitive equations. *Monthly weather review*, 91(3), 99–164.
- Sommeria, G. (1983). Numerical modeling of the planetary boundary layer. In D. K. Lilly & T. G. Chen (Eds.), (p. 681 - 704).
- Sørensen, N. N., Bechmann, A., Réthoré, P.-E., Cavar, D., Kelly, M. C., & Troen, I. (2012). How fine is fine enough when doing CFD terrain simulations. In *Ewea 2012-european wind energy conference & exhibition* (p. 1167-1172).
- Spanos, P. D., & Mignolet, M. P. (1992). Simulation of homogeneous two-dimensional random fields: Part ii—ma and arma models.
- Spronken-Smith, R., Oke, T., & Lowry, W. (2000). Advection and the surface energy balance across an irrigated urban park. *International Journal Climatol.*, 20, 1033-47.
- Steinacker, R. (1984). Area-height distribution of a valley and its relation to the valley wind. *Contr. Atmos. Phys.*, 57, 64–71.
- Stull, R. B. (1988). *An introduction to boundary layer meteorology*. Kluwer Academic Publishers.
- Sukoriansky, S., Galperin, B., & Perov, V. (2005). Application of a new spectral model of stratified turbulence to the atmospheric boundary layer over sea ice. *Bound.-Layer Meteor.*, 117, 231–257.
- Talbot, C., Bou-Zeid, E., & Smith, J. (2012). Nested mesoscale large-eddy simulations with wrf: Performance in real test cases. *JOURNAL OF HYDROMETEOROLOGY*, 13, 1421–1441.
- Temel, O., & van Beeck, J. (2017). Coupling mesoscale (wrf) to microscale simulations. In *Cfd for atmospheric flows and wind engineering*. Belgium.
- Theeuwes, N., Steeneveld, G.-J., Ronda, R., Rotach, M., & Holtslag, B. (2015, 10). Cool city mornings by urban heat. *Environmental Research Letters*, 10, 4022. doi: 10.1088/1748-9326/10/11/114022
- Thompson, G., Field, P., Rasmussen, R., & Hall, W. (2008). Explicit forecasts of winter precipitation using an improved bulk microphysics scheme. Part II: Implementation of a new snow parameterization. *Monthly Weather Review*, 136(12), 5095–5115.
- Thomson, D. W. (1986). Systems for measurements at the surface. In P. S. Ray (Ed.), *Mesoscale meteorology and forecasting* (chap. 5). American Meteorological Society.
- Troen, I., & Petersen, E. L. (1989). *European wind atlas* (Tech. Rep.). Riso National Laboratory, Roskilde, Denmark.
- Veers, P. (1988). *Three-dimensional wind simulation* (Tech. Rep.). Sandia National Labs., Albuquerque, NM (USA).

- Venkatraman, K., Hågbo, T.-O., Buckingham, S., & Giljarhus, K. E. T. (2023, January). Effect of different source terms and inflow direction in atmospheric boundary modeling over the complex terrain site of perdigão. *Wind Energy Science*, 8(1), 85–108. Retrieved from <https://doi.org/10.5194/wes-8-85-2023> doi: 10.5194/wes-8-85-2023
- Wang, W., Bruyère, C., Duda, M., Dudhia, J., Gill, D., Kavulich, M., . . . Fossell, K. (n.d.). *Wrf-arw v4: User's guide* [Manual].
- Warner, T. T. (2011). *Numerical weather and climate prediction*. Cambridge University Press.
- Whiteman, C. D. (1990). Observations of thermally developed wind systems in mountainous terrain. In W. Blumen (Ed.), *Atmospheric processes over complex terrain* (Vol. 23, chap. 45). Meteorological Monographs.
- Wicker, L. J., & Skamarock, W. C. (2002). Time splitting methods for elastic models using forward time schemes. *Mon. Wea. Rev.*, 130, 2088–2097.
- Wieringa, J. (2001). New revision of davenport roughness classification. *Proceedings of 3EACWE.Eindhoven, The Netherlands;2001.p.285–92.*
- Wood, C., & Pauscher, L. (2013). Wind observations above an urban river using a new lidar technique, scintillometry and anemometry. *SciTotalEnviron.*, 18, 527-33.
- Wyngaard, J. C. (2004). Toward numerical modeling in the “terra incognita”. *Journal of The Atmospheric Sciences*, 61, 1816–1826.
- Xu, Z., Wang, H., Zhang, H., Zhao, K., Gao, H., & Zhu, Q. (2019). Non-stationary turbulent wind field simulation of long-span bridges using the updated non-negative matrix factorization-based spectral representation method. *Applied Sciences*, 9(24), 5506.
- Zhang, X., Bao, J.-W., Chen, B., & Grell, E. D. (2018a). A three-dimensional scale-adaptive turbulent kinetic energy scheme in the wrf-arw model. *MONTHLY WEATHER REVIEW*, 46, 2023–2045.
- Zhang, X., Bao, J.-W., Chen, B., & Grell, E. D. (2018b). A three-dimensional scale-adaptive turbulent kinetic energy scheme in the wrf-arw model. *Monthly Weather Review*, 146(7), 2023–2045.
- Zhang, Z., & Moore, J. C. (2015). Data assimilation. In *Mathematical and physical fundamentals of climate change* (chap. 9). Elsevier.
- Zhao, N., & Huang, G. (2020). Wind velocity field simulation based on enhanced closed-form solution of cholesky decomposition. *Journal of Engineering Mechanics*, 146(2), 04019128.
- Zhong, J., Cai, X., & Xie, Z.-T. (2019). Implementation of a synthetic inflow turbulence generator in idealised wrf v3.6.1 large eddy simulations under neutral atmospheric conditions. *Geoscientific model development, EGU*.
- Zhou, B., Zhu, K., & Xue, M. (2017). A physically based horizontal subgrid-scale turbulent mixing parameterization for the convective boundary layer. *J. Atmos. Sci.*, 74, 2657–2674.